GEOSPHERE

GEOSPHERE, v. 14, no. 4,

https://doi.org/10.1130/GES01521.1

10 figures; 3 tables; 1 supplemental file

CORRESPONDENCE: r.halama@keele.ac.uk

CITATION: Halama, R., Glodny, J., Konrad-Schmolke, M., and Sudo, M., 2018, Rb-Sr and in situ $^{40}Ar/^{39}Ar$ dating of exhumation-related shearing and fluid-induced recrystallization in the Sesia zone (Western Alps, Italy): Geosphere, v. 14, no. 4, https://doi.org/10.1130/GES01521.1.

Science Editor: Shanaka de Silva
Guest Associate Editor: Phillipe Agard

Received 28 February 2017
Revision received 21 February 2018
Accepted 10 May 2018

Rb-Sr and in situ $^{40}Ar/^{39}Ar$ dating of exhumation-related shearing and fluid-induced recrystallization in the Sesia zone (Western Alps, Italy)

Ralf Halama[1,2], Johannes Glodny[3], Matthias Konrad-Schmolke[2,4], and Masafumi Sudo[2]

[1]School of Geography, Geology and the Environment, Keele University, Keele ST5 5BG, UK
[2]Institute of Earth and Environmental Science, University of Potsdam, Karl-Liebknecht-Str. 24-25, 14476 Potsdam, Germany
[3]GFZ German Research Centre for Geosciences, Telegrafenberg, 14473 Potsdam, Germany
[4]Department of Earth Sciences, University of Gothenburg, Guldhedsgatan 5a, 40530 Gothenburg, Sweden

ABSTRACT

The Sesia zone in the Italian Western Alps is a piece of continental crust that has been subducted to eclogite-facies conditions and records a complex metamorphic history. The exact timing of events and the significance of geochronological information are debated due to the interplay of tectonic, metamorphic, and metasomatic processes. Here we present new geochronological data using Rb-Sr internal mineral isochrons and in situ $^{40}Ar/^{39}Ar$ laser ablation data to provide constraints on the relative importance of fluid-mediated mineral replacement reactions and diffusion for the interpretation of radiogenic isotope signatures, and on the use of these isotopic systems for dating metamorphic and variably deformed rocks. Our study focuses on the shear zone at the contact between two major lithological units of the Sesia zone, the eclogitic micaschists and the *gneiss minuti*.

Metasedimentary rocks of the eclogitic micaschists unit contain phengite with step-like zoning in major element chemistry as evidence for petrologic disequilibrium. Distinct $^{40}Ar/^{39}Ar$ spot ages of relict phengite cores and overprinted rims demonstrate the preservation of individual age domains in the crystals. The eclogitic micaschists also show systematic Sr isotope disequilibria among different phengite populations, so that minimum ages of relict assemblage crystallization can be differentiated from the timing of late increments of deformation. The preservation of these disequilibrium features shows the lack of diffusive re-equilibration and underpins that fluid-assisted dissolution and recrystallization reactions are the main factors controlling the isotope record in these subduction-related metamorphic rocks.

Blueschist-facies mylonites record deformation along the major shear zone that separates the eclogitic micaschists from the *gneiss minuti*. Two Rb-Sr isochrones that comprise several white mica fractions and glaucophane constrain the timing of this deformation and accompanying near-complete blueschist-facies re-equilibration of the Rb-Sr system to 60.1 ± 0.9 Ma and 60.9 ± 2.1 Ma, respectively. Overlapping ages in eclogitic micaschists of 60.1 ± 1.1 (Rb-Sr isochron of sheared matrix assemblage), 58.6 ± 0.8, and 60.9 ± 0.4 Ma (white mica $^{40}Ar/^{39}Ar$ inverse isochron ages) support the significance of this age and show that fluid-rock interaction and partial re-equilibration occurred as much as several kilometers away from the shear zone. An earlier equilibration during high-pressure conditions in the eclogitic micaschists is recorded in minimum Rb-Sr ages for relict assemblages (77.2 ± 0.8 and 72.4 ± 1.1 Ma) and an $^{40}Ar/^{39}Ar$ inverse isochron age of 75.4 ± 0.8 Ma for white mica cores, again demonstrating that the two isotope systems provide mutually supporting geochronological information. Local reactivation and recrystallization along the shear zone lasted >15 m.y., as late increments of deformation are recorded in a greenschist-facies mylonite by a Rb-Sr isochron age of 46.5 ± 0.7 Ma.

INTRODUCTION

Geochronology in metamorphic rocks faces the difficulty that different minerals may have formed, recrystallized, and equilibrated during different times on the pressure-temperature-time (*P-T-t*) path that the rock experienced (Di Vincenzo et al., 2001; Beltrando et al., 2009; Willner et al., 2009; Warren et al., 2012a; Halama et al., 2014). The interpretation of geochronological data is further complicated by effects of deformation and fluid-rock interaction that commonly accompany distinct metamorphic stages and may cause a complete or partial resetting of the age information (Scaillet et al., 1990; Mulch et al., 2002, 2005; Putlitz et al., 2005; Warren et al., 2011; Bröcker et al., 2013). Several studies have shown that combining different geochronological methods is beneficial in unraveling the complex *P-T-t* evolution of polymetamorphosed and polydeformed rocks (Bröcker et al., 2013; Regis et al., 2014; Villa et al., 2014), but the use of combined methods relating ages and mineral growth is still relatively rare.

Here we combine Rb-Sr internal mineral isochrons, using carefully controlled mineral size fractions and texturally controlled sampling of individual

mica crystals, with in situ laser ablation $^{40}Ar/^{39}Ar$ phengite data from high-pressure metamorphosed rocks of the Sesia zone (Western Alps, Italy) to relate the geochronological information to the well-characterized petrological and geochemical evolution of these rocks. The Sesia zone (formerly also called Sesia-Lanzo zone) is a key high-pressure terrane of the Western Alps, representing a slice of continental crust that has been subducted to eclogite-facies conditions and subsequently exhumed in the hanging wall of a subducting oceanic slab. The Sesia zone has received considerable attention, and dating has been undertaken by a plethora of methods, including K-Ar (Oberhänsli et al., 1985), Rb-Sr (Oberhänsli et al., 1985; Inger et al., 1996; Cortiana et al., 1998), $^{40}Ar/^{39}Ar$ (Ruffet et al., 1995, 1997; Inger et al., 1996; Cortiana et al., 1998; Halama et al., 2014), Lu-Hf (Duchêne et al., 1997), and U-Th-Pb (Inger et al., 1996; Rubatto et al., 1999, 2011; Regis et al., 2014; Giuntoli et al., 2018b).

A key aspect that can be addressed by looking at the combined Rb-Sr internal isochrons and in situ $^{40}Ar/^{39}Ar$ data is what controls the mobility and exchange of radiogenic isotopes in mineral chronometers (Villa, 2010, 2016). The two major competing concepts are diffusion-controlled isotopic closure and dissolution-reprecipitation reactions (Villa, 2010; Romer and Rötzler, 2011). Applications of the Rb-Sr system have provided constraints on scales of isotopic homogenization, deformation-controlled equilibration, and thermochronology (Chen et al., 1996; Müller et al., 2000; Cliff and Meffan-Main, 2003; Charlier et al., 2006; Cliff et al., 2017). Moreover, Rb-Sr internal mineral isochrons have been successfully used to date fluid-rock interaction events, fluid-mediated crystallization, and deformation-induced recrystallization (Freeman et al., 1997; Glodny et al., 2002, 2003, 2008a; Walker et al., 2016). $^{40}Ar/^{39}Ar$ geochronology in metamorphic rocks has also been successfully used to date fluid-rock interaction processes (Boundy et al., 1997; Di Vincenzo and Palmeri, 2001; Warren et al., 2012b; Halama et al., 2014) as well as for determining tectonometamorphic time scales (Agard et al., 2002; Mulch et al., 2005; Di Vincenzo et al., 2006; Beltrando et al., 2009; Wiederkehr et al., 2009; Willner et al., 2009; Warren et al., 2012a; Schneider et al., 2013). In general, the importance of fluid-mediated mineral replacement reactions (Putnis, 2009) and the role of fluids and deformation in resetting geochronologic systems of minerals (Krohe and Wawrzenitz, 2000; Romer and Rötzler, 2011; Villa, 2016) have increasingly been recognized.

The main objective of this study is to test the combined approach of using Rb-Sr internal mineral isochrons and in situ $^{40}Ar/^{39}Ar$ data together with petrologic and structural information in order to constrain the relationship between age and *P-T* conditions, metasomatism, and deformation in rocks from the Sesia zone, which have experienced subduction and exhumation during the Alpine orogeny. We have selected samples from these rocks because they are well studied in their structural context and show distinct stages of metasomatic overprinting (Babist et al., 2006; Konrad-Schmolke et al., 2011a, 2011b; Halama et al., 2014; Konrad-Schmolke and Halama, 2014). We will evaluate the respective roles of dissolution-reprecipitation reactions and temperature-controlled diffusion in controlling the isotopic record of the Sesia zone samples. Ages will also be discussed in light of the regional geologic framework and tectonometamorphic history of the Sesia zone.

GEOLOGICAL SETTING

The Sesia zone is a piece of polymetamorphic continental crust of the African-Adriatic plate that was subducted and experienced eclogite-facies conditions early in the Alpine orogeny. Beltrando et al. (2010) provided a detailed account of the geological history of the Sesia zone and the Western Alps, on which the following summary is based.

Convergence between the European and Adriatic plates, the latter constituting a promontory of Africa or an independent microplate, has caused the formation of the Western Alps since the Cretaceous. The arcuate belt of the Western Alps consists of Austroalpine units (continental basement units derived from the Adriatic margin) and Penninic units (oceanic units from the Mesozoic Tethys Ocean and continental units from the European margin). The Sesia zone is a continental basement unit from the Adriatic margin and part of the Austroalpine units (Fig. 1). Today, it forms the structurally uppermost part of the Western Alps axial belt. The Sesia zone is bounded by subcontinental peridotites of the Lanzo massif to the south, by the Insubric Line and the Southern Alps to the east, and by Penninic units to the west (Fig. 1).

The Sesia zone is traditionally subdivided into three southwest-northeast–trending subunits based on lithology and metamorphic history (Fig. 1; Dal Piaz et al., 1972; Compagnoni et al., 1977). The eclogitic micaschists (EMS) consist of polymetamorphic basement that includes paragneisses, minor metabasic rocks, and marbles. During Alpine metamorphism, the EMS reached peak eclogite-facies conditions of 1.9–2.0 GPa and 550–600 °C (Babist et al., 2006, and references therein; Konrad-Schmolke et al., 2006; Regis et al., 2014). The eclogitic assemblages overprint relict Permian amphibolite-granulite assemblages in the EMS. On the retrograde *P-T* path during exhumation, the EMS was affected by a metasomatic overprint at ~1.35 GPa and 530 °C (Konrad-Schmolke et al., 2011a, 2011b). The *gneiss minuti* (GM) are also a polymetamorphic basement unit, comprising Mesozoic metasedimentary rocks, mainly meta-arkose with minor marble, calcschist, and metachert, and orthogneisses derived from Permian granitoids that intruded into the Variscan basement. The GM reached Alpine peak metamorphic conditions of 1.0–1.5 GPa at 500–550 °C and are characterized by a pervasive greenschist-facies metamorphic overprint (Compagnoni et al., 1977; Pognante et al., 1987). The *seconda zona diorito-kinzigitica* (2DK) crops out discontinuously along the contact between EMS and GM (Fig. 1). It represents a pre-Alpine slice of lower crustal, amphibolite-facies micaschists with subordinate amounts of marbles, amphibolites, and mafic granulites (Dal Piaz et al., 1971; Lardeaux et al., 1982). Re-equilibration under blueschist-facies conditions during Alpine metamorphism is restricted to the margins of the discrete slivers or to narrow shear zones (Ridley, 1989). Slightly different subdivisions of the Sesia zone have also been proposed (Venturini et al., 1994; Babist et al., 2006). Regis et al. (2014) defined the Scalaro unit as a thin cover sequence of monometamorphic terrigenous and carbonate sediments, and the Bonze unit as comprising pre-Alpine polymetamorphic metagabbros and associated quartz-rich metasediments. Importantly, it is evident that the Sesia zone contains distinct metamorphic slices, which record separate stages

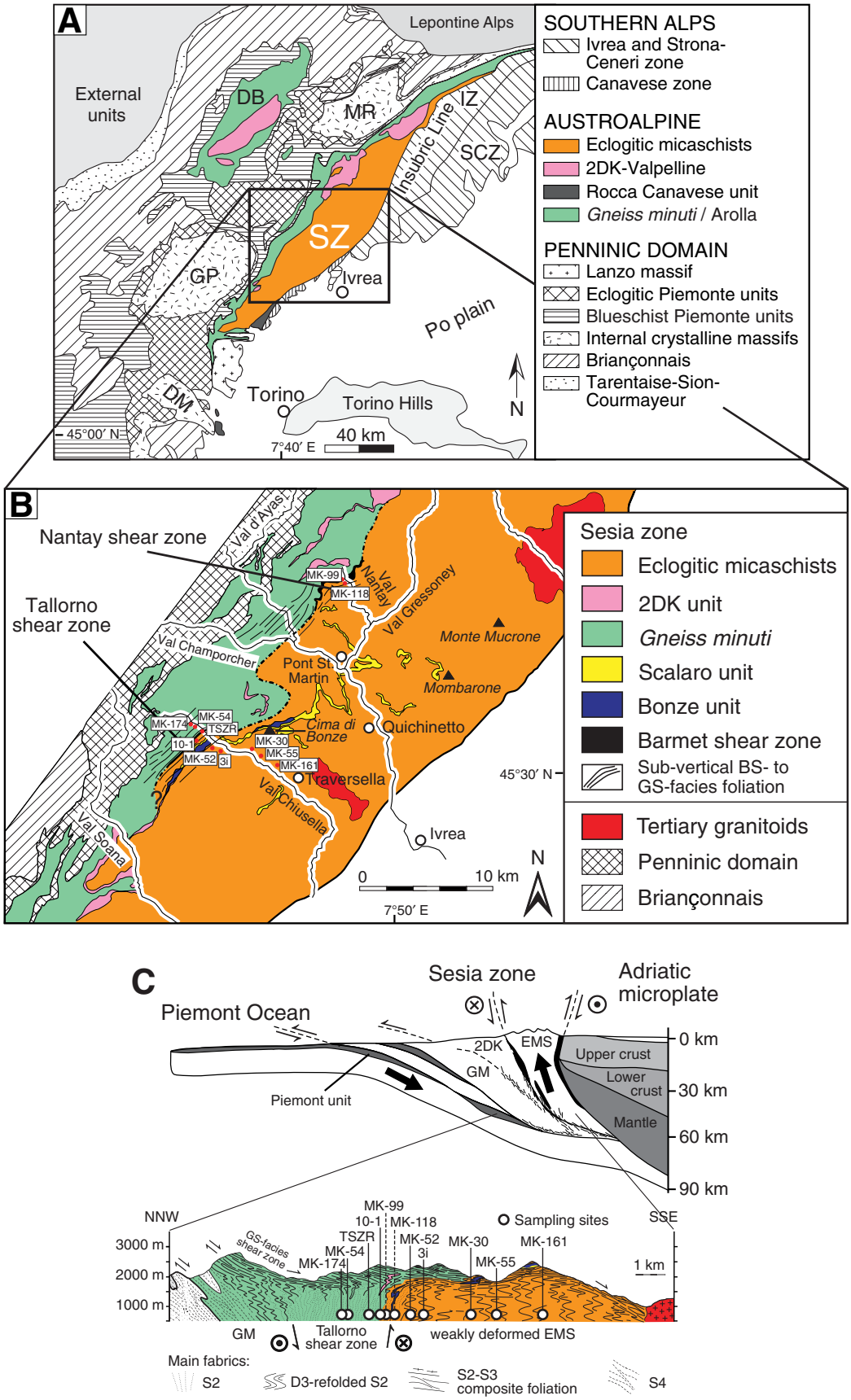

Figure 1. (A) Map of the Western Alps showing the Sesia zone (modified after Beltrando et al., 2010). Abbreviations: DB—Dent Blanche; DM—Dora Maira; GP—Gran Paradiso; IZ—Ivrea zone; MR—Monte Rosa; SCZ—Strona-Ceneri zone. (B) Detailed map of the south-central part of the Sesia zone (compiled and modified after Babist et al., 2006; Regis et al., 2014; Giuntoli and Engi, 2016). Note that the Tallorno shear zone (TSZ) and the Nantay shear zone (NSZ) are located at the boundary between eclogitic micaschists (EMS) and *gneiss minuti* (GM). Domains of the *seconda zona diorito-kinzigitica* (2DK) unit are located within the GM, whereas the Bonze and Scalaro units are located within the EMS. (C) Schematic sampling profile from the TSZ into the EMS unit along the Chiusella valley (modified from Konrad-Schmolke et al., 2011a, 2011b). Samples MK-118 and MK-99 are projected onto the cross-section as they were taken ~16 km to the northeast of the main sampling profile from the NSZ. Four samples (MK-30, MK-52, MK-55, and TSZR) are only briefly discussed in the text as they have been described and analyzed in detail in accompanying studies (see Konrad-Schmolke et al., 2011a, and Halama et al., 2014). BS—blueschist; GS—greenschist.

of deformation at eclogite-facies and blueschist- to greenschist-facies conditions (Regis et al., 2014; Giuntoli and Engi, 2016).

Juxtaposition of the two major polymetamorphic basement units of the Sesia zone, the EMS and the GM, occurred at blueschist- to greenschist-facies conditions along presently steeply dipping kilometer-scale sinistral transpressive shear zones (Babist et al., 2006; Angiboust et al., 2014; Giuntoli and Engi, 2016). These major shear zones include the Tallorno shear zone (TSZ) in the Chiusella valley (also referred to as Chiusella shear zone by Babist et al. [2006]) and the Nantay shear zone (NSZ) ~16 km to the northeast from the TSZ in the Nantay valley, a tributary to the Lys valley (Fig. 1; Konrad-Schmolke et al., 2011a; Halama et al., 2014). In these shear zones, deformation-induced recrystallization under blueschist-facies conditions caused the formation of garnet-bearing plagioclase–epidote–sodic amphibole–paragonite–phengite mylonites (Babist et al., 2006). Displacement along and fluid flow within the TSZ also caused the formation of a strain and recrystallization gradient in the adjacent EMS (Konrad-Schmolke et al., 2011a, 2011b; Giuntoli and Engi, 2016). The age of these shear zones and thus the exact timing of the juxtaposition of GM and EMS, however, is still unclear. Several samples of the TSZ and the NSZ are part of this investigation.

SAMPLE PETROGRAPHY

Samples analyzed in this study comprise two blueschist-facies mylonites from the NSZ (samples MK-99 and MK-118), two greenschist-facies mylonites from the TSZ (samples MK-54 and MK-174), and three eclogite-facies micaschists from the EMS unit (samples MK-161, 3i, and 10-1). Sample locations are shown in Figure 1, and an overview of the modal mineral contents is given in Table 1.

The blueschist-facies mylonites from the NSZ (samples MK-99 and MK-118) are fine-grained schists characterized by a strong foliation with isoclinal folding (Fig. 2A). They contain phengite + epidote + sodic amphibole + quartz + garnet + chlorite as major mineral phases and rutile + apatite + zircon + magnetite as accessories. Omphacite is lacking in all samples. Garnet is present either as small grains in the matrix or as relict porphyroblasts that are overgrown by syn-kinematically grown garnet rims. Phengite in the mylonites typically lacks petrographically or chemically distinct rims, and minerals are compositionally more homogenous than in the more weakly deformed adjacent basement units (Halama et al., 2014). Both mylonites from the NSZ equilibrated under retrograde blueschist-facies conditions and show oriented crystallization of the main blueschist-facies minerals glaucophane, phengite, and epidote parallel to the foliation (Figs. 3A, 3B). Phengites are relatively small in size (<300 μm) and have elongated crystal shapes (Fig. 4A). The rocks also show variable evidence, such as chlorite replacing garnet and chlorite + albite replacing sodic amphibole, for a later greenschist-facies overprint.

The greenschist-facies mylonites from the TSZ (samples MK-54 and MK-174) show a prominent foliation (Fig. 2B) and have a greenschist-facies main mineral assemblages of quartz + epidote + phengite + alkali feldspar + chlorite. Minor and accessory phases are titanite + apatite ± amphibole ± garnet ± albite ± zircon. The fine- to medium-grained mylonitic texture is statically overprinted, which is reflected in low-strain quartz textures with relatively straight grain boundaries and equilibrated triple junctions. Phengites typically show discrete compositional changes between pristine cores and overprinted areas (Fig. 3C). Pseudomorphs of white mica + albite after sodic amphibole and relict allanite point to an earlier metamorphic crystallization stage (Fig. 3D). Phengite occurs predominantly in grain sizes <200 μm (Fig. 4B).

The micaschists of the EMS unit (samples MK-161, 3i, and 10-1) are more weakly deformed compared to the mylonites and show a more massive appearance (Figs. 2C, 2D). Mineral phases are quartz + phengite + sodic amphibole ± garnet ± omphacite ± paragonite ± epidote ± biotite ± chlorite ± albite ± titanite ± calcite ± apatite ± zircon ± K-feldspar ± magnetite ± Fe-sulfides (Table 1). The modal proportion of phengite is >20% in all three samples. Both phengite and sodic amphibole show major-element compositional differences, with step-like compositional zoning between pristine cores and overprinted areas (Konrad-Schmolke et al., 2011a; Halama et al., 2014). The most significant feature is an increase in Fe contents in the overprinted areas, which is attributed to discrete fluid-rock interaction stages on the retrograde *P-T* path under blueschist-facies conditions (Konrad-Schmolke et al., 2011a). Subsequently, a weak greenschist-facies overprint affected the EMS samples.

Micaschist sample 10-1 was sampled in the upper Chiusella valley only a few meters away from the contact between the EMS and the TSZ, which is in this area clearly defined by shearing in the GM. The sample is characterized by alternating and deformed bands of quartz and phengite (Fig. 3E). The coarse-grained micaschist sample 3i was collected in the middle Chiusella valley from a meter-sized quartz-, sodic amphibole–, and mica-rich vein, which is subparallel to the local blueschist-facies foliation (S2 of Babist et al. [2006]). The phengite grains in this sample are up to 1 cm in size, have no preferred orientation, and texturally show distinct relict cores and overprinted rims in back-scattered electron images (cf. Konrad-Schmolke et al., 2011a). Micaschist sample MK-161, sampled in the lower Chiusella valley, shows two distinct textural domains, an omphacite-rich, eclogite-facies microlithon with centimeter-sized omphacite grains and a post–eclogite facies, sheared matrix (Fig. 3F). The omphacite-dominated microlithons comprise large (up to 1 mm in size) phengite flakes (Figs. 3G, 3H). Large phengite flakes (>500 μm) are a characteristic feature of the EMS samples in general. They coexist with a population of significantly smaller (<300 μm) and more elongated phengites (Figs. 4C, 4D).

ANALYTICAL METHODS

Rb-Sr Isotope Analyses

Rubidium-strontium (Rb-Sr) isotope work was carried out at the GFZ (German Research Centre for Geosciences), Potsdam. Sample preparation and

TABLE 1. MINERALOGY OF THE SESIA ZONE SAMPLES (WESTERN ALPS, ITALY)

Sample	Rock type	Sample coordinates	Major mineral phases	Accessory minerals
MK-174	Greenschist-facies mylonite	45.5475°N, 7.6496°E	Quartz (35%) Phengite (15%) Alkali feldspar (15%) Garnet (15%) Chlorite (10%) Epidote (10%)	Allanite Titanite Apatite Zircon Amphibole Opaques
MK-54	Greenschist-facies mylonite	45.5468°N, 7.6518°E	Quartz (50%) Phengite (25%) Epidote (20%) Alkali feldspar (5%)	Chlorite Apatite Titanite Opaques Albite
MK-118	Blueschist-facies mylonite	45.6507°N, 7.7979°E	Quartz (30%) Epidote (30%) Phengite (15%) Amphibole (10%) Garnet (10%) Chlorite (5%)	Rutile Apatite Zircon Opaques
MK-99	Blueschist-facies mylonite	45.6449°N, 7.7976°E	Phengite (20%) Amphibole (15%) Garnet (15%) Paragonite (15%) Epidote (12%) Albite (10%) Quartz (8%) Chlorite (5%)	Apatite Titanite Rutile Opaques
10-1	Eclogitic micaschist	45.5328°N, 7.6491°E	Quartz (45%) Phengite (25%) Carbonate (10%) Amphibole (5%) Paragonite (5%) Chlorite (5%) Opaques (5%)	Rutile Titanite Apatite Alkali feldspar Biotite
3i	Eclogitic micaschist	45.5328°N, 7.6755°E	Phengite (35%) Quartz (30%) Garnet (20%) Epidote (5%) Carbonate (4%) Chlorite (3%) Amphibole (3%)	Rutile Titanite Biotite Apatite Opaques
MK-161	Eclogitic micaschist	45.5159°N, 7.7299°E	Quartz (50%) Phengite (30%) Amphibole (8%) Omphacite (5%) Alkali feldspar (5%) Albite (2%)	Epidote Titanite Biotite Zircon Apatite Opaques

Note: Modal proportions of minerals were estimated based on petrographic observations and back-scattered electron images. Abundances of major minerals were normalized to 100%.

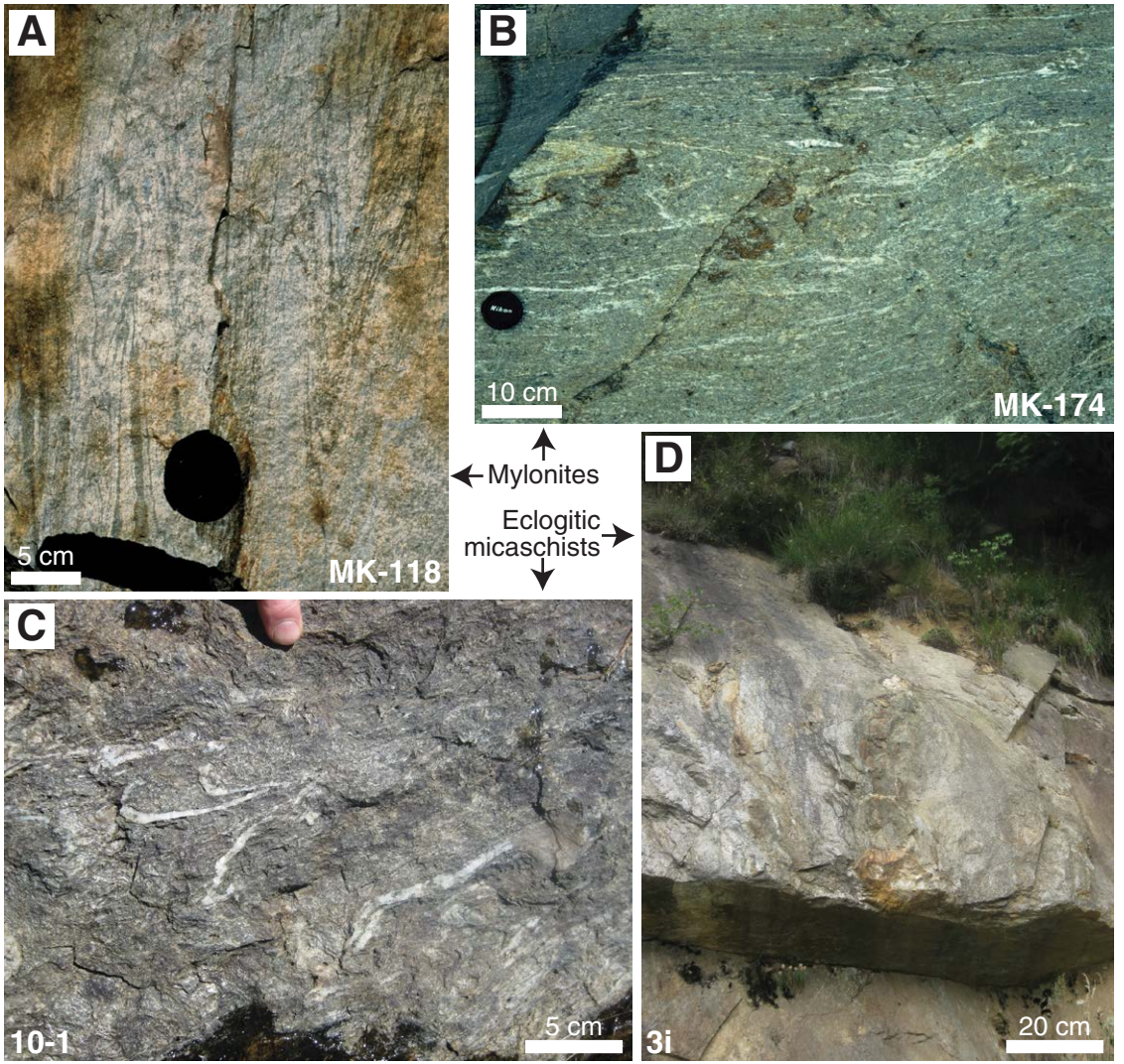

Figure 2. Field observations from the sample locations. (A) Blueschist-facies mylonite from the Nantay shear zone with isoclinal folding. The black shapes are random color blobs. (B) Greenschist-facies mylonite from the Tallorno shear zone. (C) Eclogitic micaschist from the upper Chiusella valley with deformed quartz bands. (D) Massive eclogitic micaschist from the middle Chiusella valley with a vein subparallel to the foliation.

analytical procedures followed the methods described by Glodny et al. (2008a), which are briefly summarized here. We employed the Rb-Sr internal mineral isochron approach using both bulk mineral separates and individual minerals from specific domains within the samples. Different minerals were separated based on distinct magnetic properties and grain sizes. Microdrilling of specific areas in white mica was carried out as well but did not yield sufficient amounts of sample material for accurate isotope analyses. To obtain the mineral separates, samples were first carefully disintegrated to retain the original grain size distribution of the white mica population. Then, the samples were sieved to separate the different white mica populations based on grain size. All mineral separates were visually checked and purified by handpicking under the binocular microscope, generally avoiding material with alteration. Only after that separation, white mica grain size fractions were carefully grinded in a polished agate mortar and washed. These procedures ensured that any inclusions

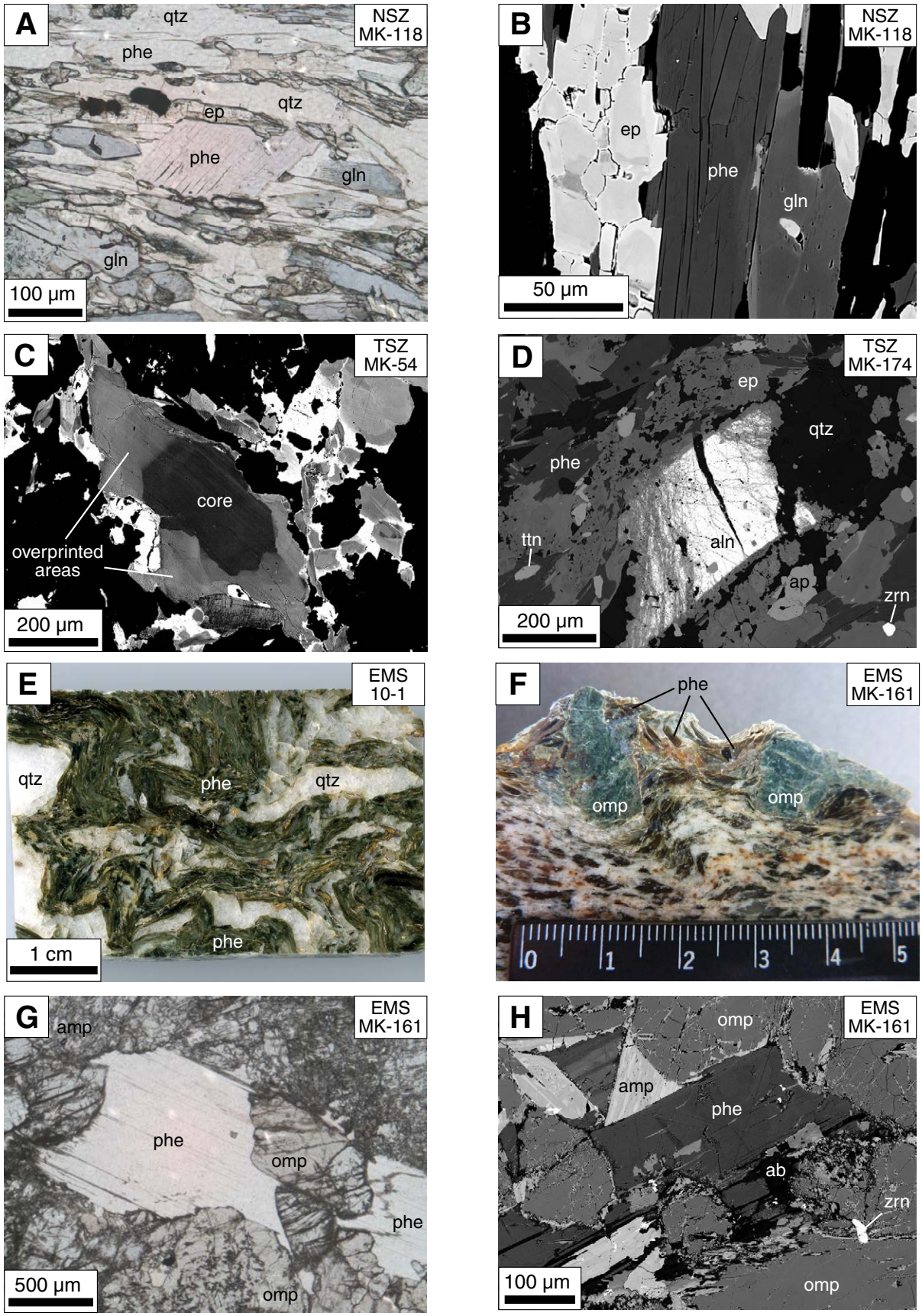

Figure 3. Representative sample images of the mylonites (A–D) and the eclogitic micaschists (EMS) (E–H). (A) Thin section microphotograph in plain polarized light (PPL) of a blueschist-facies assemblage in a mylonite from the Nantay shear zone (NSZ) (sample MK-118) with glaucophane (gln) + phengite (phe) + quartz (qtz) + epidote (ep). (B) Back-scattered electron (BSE) image of the major minerals defining the mylonitic fabric in sample MK-118. (C) BSE image of a greenschist-facies mylonite (sample MK-54) showing a large phengite grain with relict core and overprinted rims. (D) BSE image of a greenschist-facies mineral assemblage in a mylonite from the Tallorno Shear Zone (TSZ) (sample MK-174) with phengite + epidote + titanite (ttn) + quartz + apatite (ap) + zircon (zrn) + allanite (aln). (E) Photograph of an EMS (sample 10-1) with interlayering of quartz-rich and phengite-rich bands. (F) Hand specimen photograph of an EMS (sample MK-161) with large omphacite (omp) aggregates and relatively undisturbed phengite flakes. Scale is in centimeters. (G) Thin section microphotograph (PPL) of sample MK-161 showing large phengite flakes with omphacite and subordinate fine-grained amphibole (amp). (H) BSE image of sample MK-161 with phengite, omphacite, amphibole, albite (ab), and zircon.

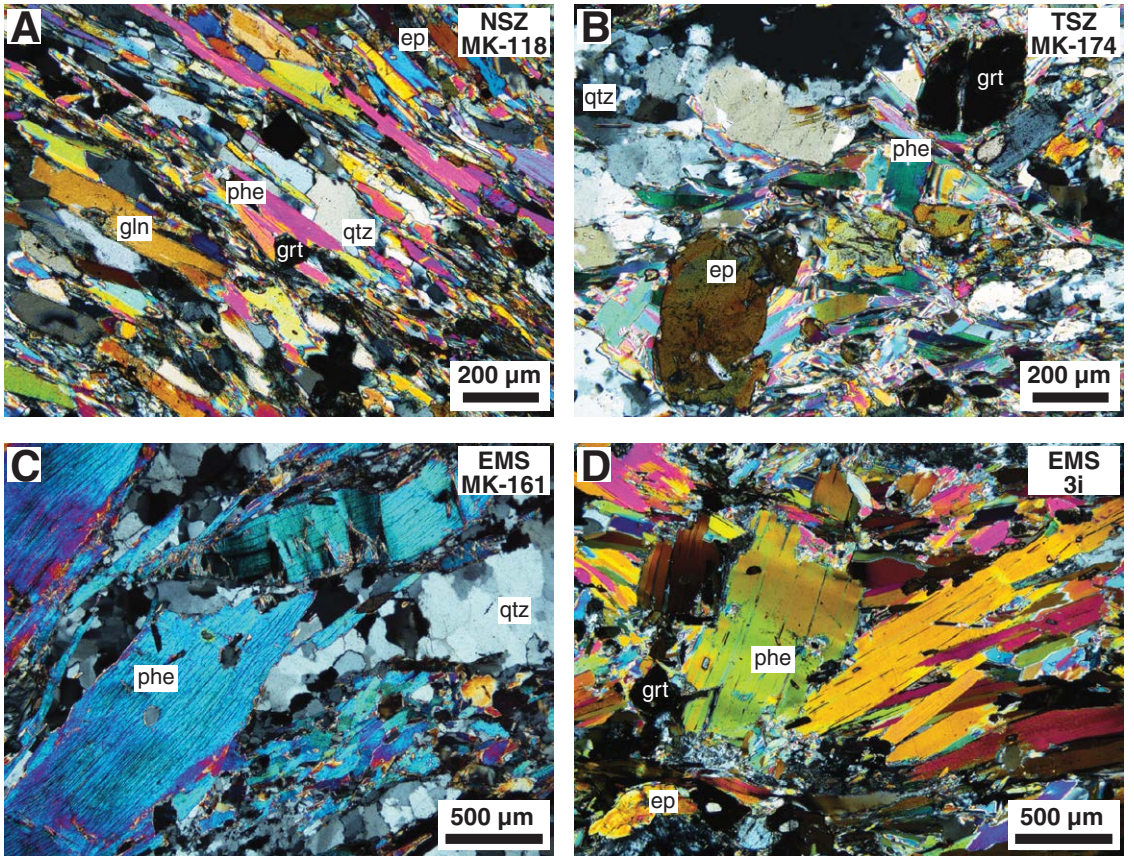

Figure 4. Thin section microphotographs in cross-polarized light to illustrate the size distribution of phengite in the Sesia zone samples. (A) Blueschist-facies mylonite, Nantay shear zone (NSZ). (B) Greenschist-facies mylonite, Tallorno shear zone (TSZ). (C, D) Eclogitic micaschists (EMS). ep—epidote; gln—glaucophane; grt—garnet; phe—phengite; qtz—quartz.

larger than a few micrometers and any other non-micaceous material were removed from the mica separate and that Rb-Sr signatures of the various white mica grain size fractions were preserved as well as possible. Typical sample weights were 5–15 mg for white mica, 30 mg for glaucophane, omphacite, and quartz-feldspar concentrates, and 2–10 mg for low-Rb/Sr phases (phases with low Rb/Sr ratios, e.g., apatite, epidote).

Rubidium and Sr concentrations were determined by isotope dilution using mixed ^{87}Rb-^{84}Sr spikes. Samples were dissolved in a mixture of HF and HNO_3 and then evaporated to dryness, with formation of fluoride salts. By addition of 6N HCl and subsequent evaporation to dryness, the fluorides were converted to chlorides. Chlorides were taken up in 2.5N HCl and processed by standard HCl-based cation exchange techniques. Rb and Sr isotope ratios were measured using a Thermo Scientific Triton thermal ionization mass spectrometer. Sr isotopic composition was measured in dynamic multicollection mode. Rb isotope dilution analysis was done in static multicollection mode. Total procedural blanks were consistently <0.15 ng for both Rb and Sr. Because of generally low blank-to-sample ratios and highly variable blank values, no blank correction was applied. The value obtained for ^{87}Sr/^{86}Sr in the U.S. National Institute of Standards and Technology (NIST) SRM 987 isotopic standard during the period of analytical work was 0.710242 ± 0.000005 (2σ, n = 16). For age calculation, standard uncertainties, as derived from replicate analyses of spiked white mica samples, of ±0.005% for ^{87}Sr/^{86}Sr and of ±1.5% for ^{87}Rb/^{86}Sr ratios were assigned to the results, provided that individual analytical uncertainties were smaller than these values. Otherwise, individual analytical uncertainties were used. Uncertainties of isotope and age data are quoted at 2σ throughout this work. The program Isoplot/Ex 3.71 (Ludwig, 2009) was used to calculate regression lines.

The ^{87}Rb decay constant $\lambda = 1.3972 \pm 0.0045 \times 10^{-11}$ a^{-1} is used as recommended by the International Union of Pure and Applied Chemistry–International Union of Geological Sciences (IUPAC-IUGS) (Villa et al., 2015).

In Situ $^{40}Ar/^{39}Ar$ Analyses

Argon-argon ($^{40}Ar/^{39}Ar$) dating was performed at the Institute of Earth and Environmental Science, University of Potsdam, following analytical methods described by Wiederkehr et al. (2009) and Halama et al. (2014). In brief, polished thick sections were irradiated with fast neutrons at a flux rate of 1×10^{13} n cm^{-2} s^{-1} for 10 h at NRG Petten, Netherlands. FC3 sanidine from the Fish Canyon Tuff was irradiated as a neutron flux monitor and to derive J-values. We use an age of 27.5 Ma for the FC3 sanidine to maintain consistency with a previous study (see Halama et al. [2014] for details), which is based on the agreement between the K-Ar ages determined by the Geological Survey of Japan (Uto et al., 1997) and by the U.S. Geological Survey based on first principles calibration (Lanphere and Baadsgaard, 2001). To facilitate correction for Ar isotope interferences produced by reactions of the neutron flux with K or Ca in the samples, K_2SO_4 and CaF_2 crystals were irradiated along with the samples.

The Ar isotopic analytical line consists of a New Wave Gantry Dual Wave laser ablation system, a frequency-quadrupled laser wavelength of 266 nm, an ultrahigh-vacuum purification line, and a Micromass 5400 noble gas mass spectrometer. The laser was operated with a repetition rate of 10 Hz and a beam size of 50–80 μm. For gas extraction from the samples, a continuous ablation for 2 min was performed. Complex zigzag patterns were occasionally adopted to avoid visible inclusions and cracks on the mineral surfaces and to ablate areas as large as possible to maximize the Ar signal. Back-scattered electron images of the thick sections were used to select the most suitable locations for the in situ Ar isotopic analyses. The extracted gas was purified in the ultrahigh-vacuum line via SAES getter pumps and a cold trap for 10 min. The high-sensitivity, low-background sector-type mass spectrometer is equipped with an electron multiplier pulse counting system for analyzing small amounts of Ar. Blanks were run at the start of each session and after every three unknowns. The raw data were corrected for procedural blank contributions, mass discrimination by analysis of atmospheric Ar, decay of radioactive ^{37}Ar and ^{39}Ar isotopes produced by irradiation, and interferences of ^{36}Ar, ^{39}Ar, and ^{40}Ar produced from ^{40}Ca, ^{42}Ca, and ^{40}K, respectively. Atmospheric ratios of 295.5 for $^{40}Ar/^{36}Ar$ and 0.1869 for $^{38}Ar/^{36}Ar$ were used for atmospheric and mass discrimination corrections (Nier, 1950; Steiger and Jäger, 1977). Decay constants of 5.543×10^{-10} a^{-1} for total ^{40}K, 1.978×10^{-2} d^{-1} for ^{37}Ar, and 2.58×10^{-3} a^{-1} for ^{39}Ar were used for age calculations. Age and error calculation procedures are described by Uto et al. (1997). For the inverse isochron ($^{36}Ar/^{40}Ar$ versus $^{39}Ar/^{40}Ar$) diagrams, we use mean square weighted deviation (MSWD) and probability of occurrence (p) as statistical parameters to evaluate the reliability of the inverse isochron age information (Wendt and Carl, 1991; Baksi, 1999, 2006; Ludwig, 2009). Values for $p > 0.05$ are considered as acceptable, whereas excess scatter of data points relative to the expected scatter is demonstrated for $p < 0.05$ (Baksi, 2006).

RESULTS

Rb-Sr Internal Mineral Isochrons

Internal mineral isochrons were determined for five samples, comprising two blueschist-facies mylonites (samples MK-118 and MK-99) from the NSZ, one greenschist-facies mylonite (sample MK-174) from the TSZ, and two micaschists from the EMS unit (samples 3i and MK-161). The complete set of Rb-Sr isotopic data is given in Table 2.

Blueschist-Facies Mylonites

The two mylonites with blueschist-facies mineral assemblages from the NSZ provide an age for the blueschist-facies sinistral transpressive deformation. A seven-point isochron for sample MK-118 yields an age of 60.1 ± 0.9 Ma (Fig. 5A), whereas a six-point isochron for sample MK-99 gives 60.9 ± 2.1 Ma (Fig. 5B). Both isochrons include glaucophane and several white mica fractions. There is no obvious correlation between white mica grain size and apparent ages for the respective fractions.

Greenschist-Facies Mylonites

The greenschist-facies mineral assemblage in the mylonite from the TSZ (sample MK-174) shows evidence for Sr isotopic disequilibria in the white mica population. A regression line based on all seven points yields an age of 47.6 ± 3.4 Ma (Fig. 5C). However, the finest white mica fraction (125–90 μm) plots below the regression line, whereas the largest white mica fraction (>250 μm) plots above the regression line. Moreover, the low-Rb/Sr phases epidote, apatite, and allanite have distinct Sr isotopic compositions. Based on petrographic observations, allanite is a relict phase not in equilibrium with the surrounding matrix minerals (Fig. 3D). Hence, a minimum age for the relict assemblage of 55.7 ± 0.8 Ma can be calculated based on combining the white mica fraction with the largest grain size (>250 μm) with allanite.

A maximum age for the end of the deformation of 46.5 ± 0.7 Ma is obtained from the finest-grained white mica fraction (125–90 μm fraction) and recrystallized apatite. The age brackets derived from this analysis have no direct geological significance ("mixed ages") but nevertheless provide useful information in the assessment of the geochronological evolution of the Sesia zone.

TABLE 2. Rb-Sr ANALYTICAL DATA FOR SESIA ZONE SAMPLES (WESTERN ALPS, ITALY)

Sample no.	Material	Rb (ppm)	Sr (ppm)	$^{87}Rb/^{86}Sr$	$^{87}Sr/^{86}Sr$	$^{87}Sr/^{86}Sr$ $2\sigma_m$ (%)
Eclogitic micaschist complex: Micaschist						
3i (59.4 ± 3.1 Ma, MSWD = 21, Sr_i = 0.71046 ± 0.00012, *n* = 7)						
	White mica 250–160 µm	355	194	5.28	0.714783	0.0028
	White mica 500–355 µm	353	262	3.90	0.713707	0.0015
	White mica >1000 µm	344	333	3.00	0.713036	0.0020
	Calcite	10.9	284	0.110	0.710579	0.0013
	Apatite	0.19	3765	0.00015	0.710333	0.0010
	Epidote	2.96	3061	0.00279	0.710560	0.0018
	Titanite concentrate	63.4	172	1.07	0.711303	0.0034
Eclogitic micaschist complex: Eclogite-facies assemblage						
MK-161 (68.0 ± 2.4 Ma, MSWD = 740, Sr_i = 0.7271 ± 0.0029, *n* = 6)						
(72.4 ± 1.1 Ma = minimum age for eclogite facies imprint, E-omp1 + E-wm3)						
	Omphacite (E-omp1)	21.2	169	0.363	0.726952	0.0016
	Omphacite (E-omp2)	5.82	177	0.0951	0.728087	0.0018
	White mica (E-wm3)	486	42.2	33.5	0.760474	0.0015
	White mica (E-wm2)	520	10.7	143	0.861216	0.0021
	White mica (E-wm1) >1000 µm	533	9.99	157	0.878240	0.0045
	White mica (E-wm1) <1000 µm	509	26.6	55.7	0.777812	0.0023
Eclogitic micaschist complex: Post–eclogite facies micaschist						
MK-161 (60.1 ± 1.1 Ma, MSWD = 8554, Sr_i = 0.7363 ± 0.0011; fine-grained white mica, apatite, titanite; *n* = 5)						
(77.2 ± 0.8 Ma = minimum age for relict assemblage, epidote + white mica 5–3 mm; *n* = 3)						
	White mica 5–3 mm (I)	494	15.2	95.2	0.834199	0.0139
	White mica 5–3 mm (II)	494	13.6	107	0.845277	0.0059
	White mica 500–355 µm	486	10.3	138	0.860431	0.0043
	White mica 250–160 µm (I)	482	8.47	167	0.877841	0.0031
	White mica 250–160 µm (II)	485	8.84	161	0.872345	0.0367
	White mica >2.82 g cm^{-3}	485	16.2	87.3	0.808696	0.0018
	Apatite	2.17	3231	0.00195	0.736119	0.0014
	Titanite	17.9	488	0.106	0.736703	0.0028
	Quartz-albite	7.15	51.1	0.406	0.732969	0.0026
	Epidote	0.35	12,932	0.00008	0.730910	0.0009
Nantay shear zone: Blueschist-facies mylonite						
MK-118 (60.1 ± 0.9 Ma, MSWD = 13, Sr_i = 0.71169 ± 0.00019, *n* = 7)						
	White mica 160–90 µm	343	29.9	33.4	0.739442	0.0180
	White mica 250–160 µm	340	31.7	31.1	0.737703	0.0081
	White mica 355–250 µm	350	32.6	31.1	0.738003	0.0033
	White mica 500–355 µm	277	81.9	9.78	0.720098	0.0018
	Glaucophane	6.67	27.0	0.715	0.712157	0.0021
	Apatite	0.83	240	0.0100	0.711653	0.0012
	Epidote	5.41	1044	0.0150	0.711751	0.0031
Nantay shear zone: Blueschist-facies mylonite						
MK-99 (60.9 ± 2.1 Ma, MSWD = 9, Sr_i = 0.71166 ± 0.00044, *n* = 7)						
	White mica 125–90 µm	303	74.7	11.8	0.721295	0.0025
	White mica 250–160 µm	357	36.3	28.5	0.735693	0.0035
	White mica >250 µm	355	40.0	25.7	0.733985	0.0011
	Feldspar-quartz	2.88	15.0	0.555	0.712193	0.0070
	Apatite	1.92	296	0.0188	0.711761	0.0028
	Glaucophane concentrate	37.9	259	0.424	0.712055	0.0015
Tallorno shear zone: Greenschist-facies mylonite						
MK-174 (47.6 ± 3.4 Ma, MSWD = 82, Sr_i = 0.7128 ± 0.0014, *n* = 7)						
(46.5 ± 0.7 Ma = maximum age for end of deformation; apatite + white mica 125–90 µm)						
(55.8 ± 0.8 Ma = minimum age of relict assemblage; allanite + white mica >250 µm)						
	White mica > 250 µm	305	52.9	16.7	0.725167	0.0021
	White mica 250–160 µm	304	30.8	28.6	0.732945	0.0022
	White mica 160–125 µm	305	20.3	43.5	0.742202	0.0039
	White mica 125–90 µm	302	15.4	57.0	0.749348	0.0020
	Epidote	7.35	1540	0.0138	0.712460	0.0015
	Apatite	1.55	807	0.00557	0.712286	0.0048
	Allanite	9.63	1199	0.0233	0.712174	0.0014

Abbreviations: MSWD—Mean square weighted deviation; Sr_i—initial $^{87}Sr/^{86}Sr$ isotope ratio.
Note: In sample MK-161, white mica >2.82 g cm^{-3} was separated from the material >500 µm to obtain a fraction of relatively Fe-rich white mica.

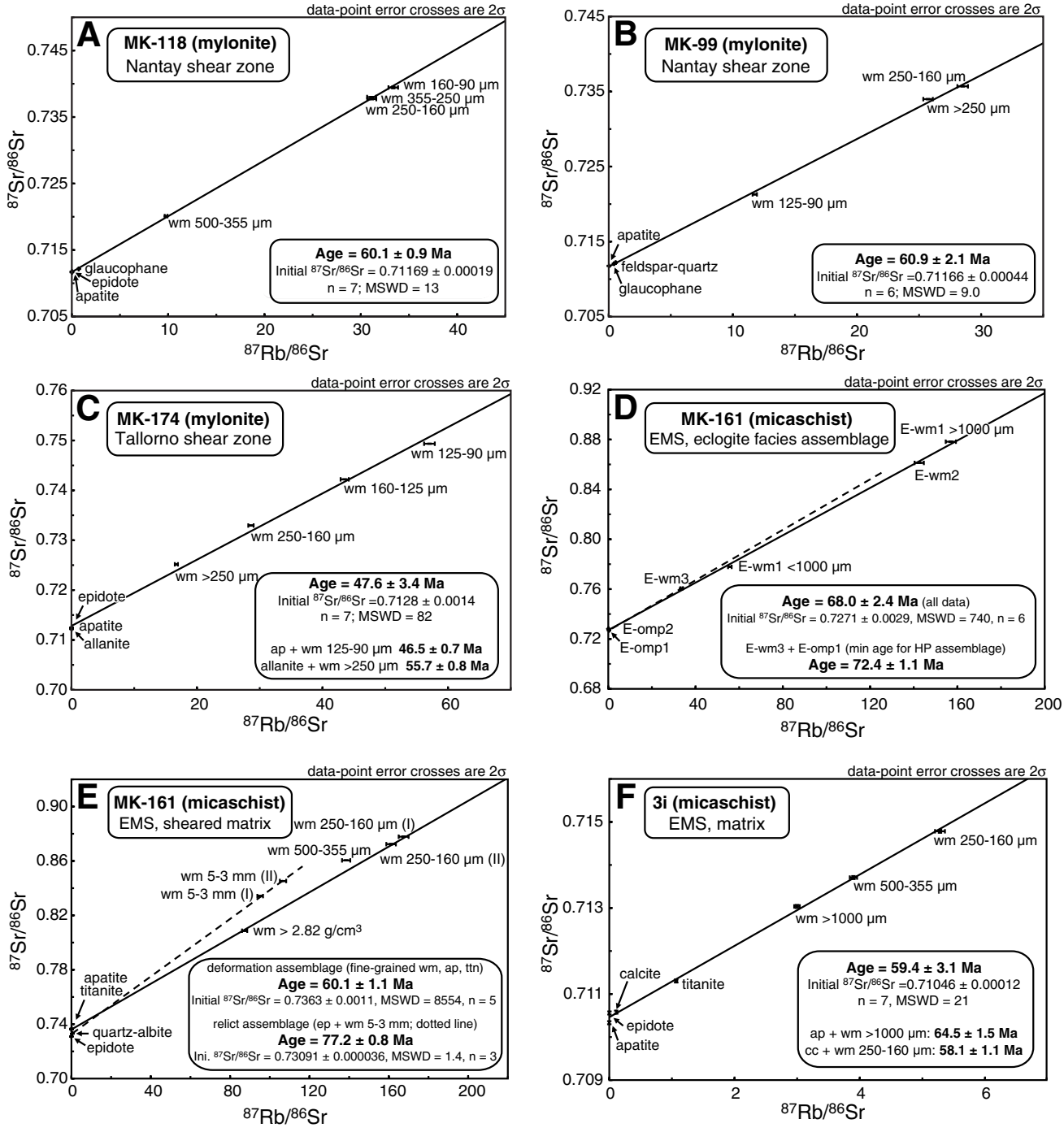

Figure 5. Rb-Sr isochron diagrams for the investigated mylonites from the Nantay (A, B) and Tallorno (C) shear zones and for micaschists from the eclogitic micaschists (EMS) unit (D–F). I and II indicate that specific mineral size fractions have been split into two separate fractions for analysis. ap—apatite; cc—calcite; E—minerals separated from the eclogitic microlithon; ep—epidote; omp—omphacite; ttn—titanite; wm—white mica; MSWD—mean square weighted deviation. Analytical data and details about the mineral fractions shown are presented in Table 2.

Eclogitic Micaschists (EMS)

Micaschist sample MK-161 was subdivided into two distinct domains, an omphacite-rich, eclogite-facies microlithon and a post–eclogite facies, sheared matrix (Fig. 6A). For the eclogite-facies microlithon, a six-point regression line yields an apparent age of 68.0 ± 2.4 Ma, which reflects Sr isotope disequilibria (Fig. 5D). Assuming that the minerals were variably affected by post–eclogite facies re-equilibration causing the isotope disequilibria, the apparently oldest omphacite (E-omp1, with the least-radiogenic Sr isotopic composition) and white mica (E-wm3) were combined to give a minimum age for the eclogite-facies stage of 72.4 ± 1.1 Ma.

The sheared matrix of the micaschist MK-161 also provides age information about the relict eclogite-facies assemblage and subsequent deformation (Fig. 5E). Strontium isotopic disequilibria are evident in a positive correlation between white mica grain size and apparent ages. Moreover, differences in the Sr isotopic compositions of the low-Rb/Sr phases epidote and titanite-apatite show a significantly lower $^{87}Sr/^{86}Sr$ isotope ratio for epidote. A five-point regression line based on three fine-grained white mica fractions, apatite, and titanite yields and age of 60.1 ± 1.1 Ma. A minimum age for the relict assemblage defined by epidote and two coarse-grained white mica fractions (3–5 mm) is 77.2 ± 0.8 Ma.

Micaschist sample 3i also provides ample evidence of Sr isotope disequilibria, similar to micaschist MK-161, showing the grain size–apparent age correlation in the different white mica fractions and distinct $^{87}Sr/^{86}Sr$ ratios of the low-Rb/Sr phases calcite, epidote, and apatite (Fig. 5F). The regression line of all seven data points yields an age of 59.4 ± 3.1 Ma. A maximum age for the end of ductile deformation of 58.1 ± 1.1 Ma can be derived by combining fine-grained white mica (250–160 µm) with calcite. The minimum age for the relict assemblage is 64.5 ± 1.5 Ma based on combining apatite with white mica >1000 µm.

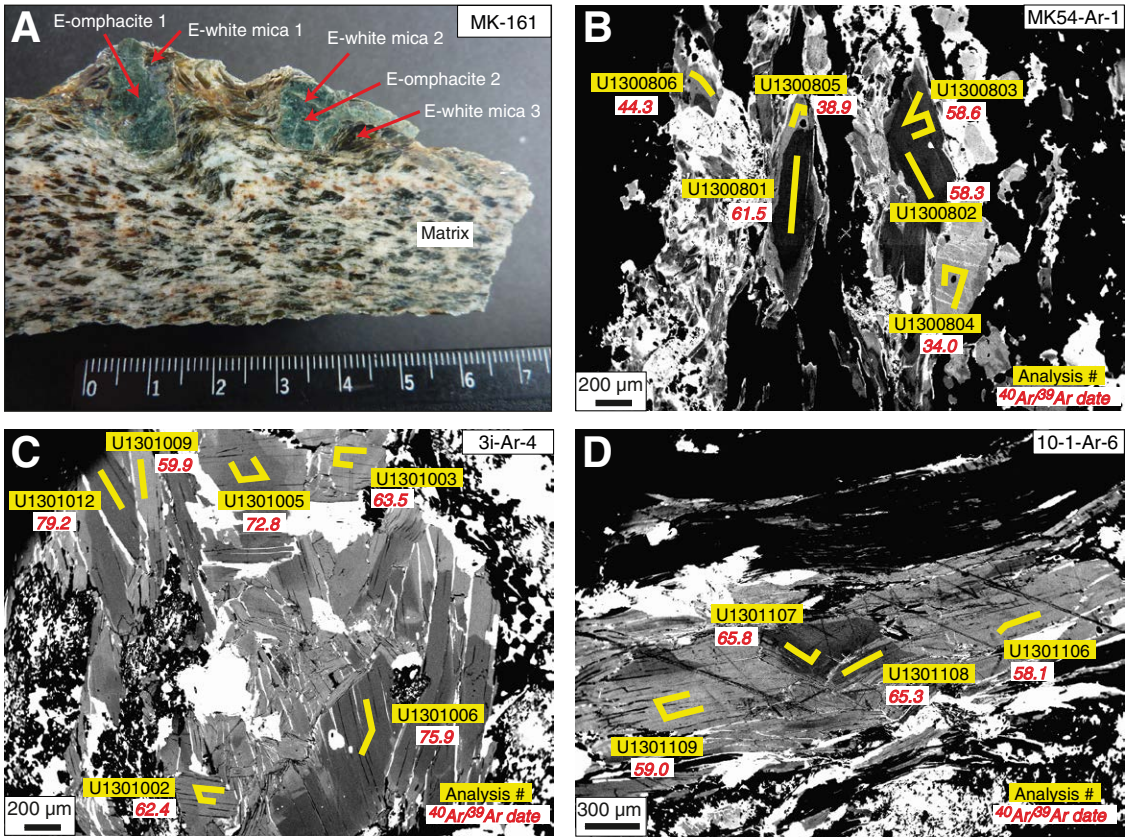

Figure 6. Spatial information about the sampling for geochronological investigations. (A) Distinct sample domains in micaschist MK-161, illustrating the locations where minerals for dating the eclogite-facies assemblage (prefix "E") by Rb-Sr were separated. Scale is in centimeters. (B–D) Back-scattered electron images of phengite in samples MK-54 (B), 3i (C), and 10-1 (D) with locations of laser lines (yellow) for in situ $^{40}Ar/^{39}Ar$ analyses. Ages are given in italics (in Ma). Note the distinct difference between dark, relict core regions compared to light, overprinted domains. See Table 3 for complete data set.

In Situ $^{40}Ar/^{39}Ar$ Geochronology

Four samples were investigated by in situ $^{40}Ar/^{39}Ar$ geochronology, comprising one blueschist-facies mylonite (sample MK-99), one greenschist-facies mylonite (sample MK-54), and two micaschists from the EMS unit (samples 10-1 and 3i). The analyses expand on an accompanying study (Halama et al., 2014), where a sample profile across the TSZ was investigated, and geochronological data from three samples of the EMS unit (samples MK-30, MK-52, and MK-55) and one mylonite (sample TSZR) from that study will be incorporated into the discussion. In situ $^{40}Ar/^{39}Ar$ ages are presented in Table 3, and the complete set of Ar isotopic data is given in the Supplemental File[1].

Blueschist-Facies Mylonites

The 19 in situ analyses of mylonite MK-99 show a broad range in apparent $^{40}Ar/^{39}Ar$ ages from ca. 111 to ca. 82 Ma (Table 3). All but one of the samples fall into the more restricted interval of 100–82 Ma, with an average for this group of 87.5 ± 4.3 Ma. However, as shown in our accompanying study (Halama et al., 2014), inverse isochron calculations yield statistically unreliable ($p \leq 0.01$) ages of 81.6 ± 1.4 and 62.3 ± 2.6 Ma with initial $^{40}Ar/^{36}Ar$ ratios of 417 ± 31 and 954 ± 114.

Greenschist-Facies Mylonites

Thirty-six in situ analyses were carried out in the greenschist-facies mylonite sample MK-54, 18 in relict core areas and 18 in metasomatically overprinted areas (Table 3; Fig. 7). Overall, apparent $^{40}Ar/^{39}Ar$ ages range from ca. 67 to ca. 33 Ma. There is a clear distinction between relict core ages (range 67.2–58.3 Ma, average 60.9 ± 2.3 Ma) and overprinted rim domains (range 57.7–32.8 Ma, average 43.9 ± 7.3 Ma; Fig. 6B), but the age frequency distribution of the two domains is completely different. The relict cores have two outliers with older ages of ca. 65 and ca. 67 Ma (Fig. 7A). With the exception of these outliers, the core apparent $^{40}Ar/^{39}Ar$ ages are tightly clustered in the range 58.3–62.5 Ma (average 60.3 ± 1.3 Ma). The corresponding inverse isochron is well defined and statistically reliable ($p = 0.211$), yielding an age of 60.9 ± 0.4 Ma and an initial $^{40}Ar/^{36}Ar$ ratio within ~5% uncertainty of the atmospheric ratio (Fig. 7B). In contrast, apparent $^{40}Ar/^{39}Ar$ ages of the overprinted rims scatter widely from ca. 58 to ca. 33 Ma (Fig. 7C). Accordingly, the inverse isochron diagram shows significant scatter, too, resulting in an extremely low statistical reliability ($p = 0.000$) for the inverse isochron (Fig. 7D).

Eclogitic Micaschists (EMS)

In situ analyses of micaschist 3i show a distinct separation of relict core and overprinted rim ages (Fig. 6C; Table 3). Apparent $^{40}Ar/^{39}Ar$ ages of relict cores exhibit a spread from 82 to 64 Ma (average 75.4 ± 3.6 Ma), but all except one data point fall into the range 70–82 Ma. Overprinted rims are distinctly younger and yield apparent $^{40}Ar/^{39}Ar$ ages from 57 to 69 Ma (average 62.4 ± 3.7 Ma). Sample section 3i-Ar-4 nicely exemplifies this distinction between core and rim ages (Fig. 8). Apparent $^{40}Ar/^{39}Ar$ ages of relict cores cluster around ca. 75–76 Ma with two outliers at 72.8 and 79.2 Ma (Fig. 8A). The inverse isochron age of six cores (outliers excluded) is 75.4 ± 0.8 Ma with an initial $^{40}Ar/^{36}Ar$ ratio of 312 ± 69, overlapping the atmospheric ratio (Fig. 8B). The high p value of 0.785 indicates a high statistical reliability of this inverse isochron. Overprinted rims in sample section 3i-Ar-4 show a larger scatter in the range ca. 60–66 Ma without any outliers (Fig. 8C). The corresponding inverse isochron age is 60.2 ± 1.4 Ma with an acceptable p value of 0.285 and a poorly defined initial $^{40}Ar/^{36}Ar$ value of 442 ± 102 (Fig. 8D).

The 26 in situ analyses of micaschist 10-1 yield apparent $^{40}Ar/^{39}Ar$ ages that range from ca. 69 to ca. 55 Ma (Table 3). There is a clear difference in age between the 14 relict cores (range 69.1–61.5 Ma, average 64.9 ± 2.3 Ma) and the 12 metasomatically overprinted rims (range 62.8–54.7 Ma, average 58.7 ± 2.1 Ma; Fig. 6D). No outliers can be identified for the cores (Fig. 8E), which yield a poorly defined and statistically unreliable ($p = 0.002$) inverse isochron age of 66.3 ± 0.5 Ma (Fig. 8F). The overprinted rims of micaschist 10-1 show a small spread in ages, with 10 of the 12 analyses falling between ca. 56 and ca. 61 Ma (Fig. 8G). These data yield a well-defined inverse isochron age of 58.6 ± 0.8 Ma with a high statistical reliability ($p = 0.465$) and an initial $^{40}Ar/^{36}Ar$ ratio overlapping the atmospheric value (Fig. 8H). In summary, the overprinted rim inverse isochron ages for the two eclogitic micaschists overlap at ca. 60 Ma, whereas the relict cores ages differ by ~10 m.y.

DISCUSSION

Rb-Sr Data: Age Information versus Mixing

The Rb-Sr internal mineral isochron methodology allows the identification of Sr isotopic equilibrium-disequilibrium relationships between different minerals and mineral assemblages (Glodny et al., 2008a). In all analyzed samples, we observe a more or less marked spread in Rb/Sr ratios between different mica grain size fractions. We interpret this spread as largely reflecting variations in the trace element signatures of the analyzed white mica, caused by changing pressure, temperature, and microchemical environments during mica crystallization. Thus, we regard the variable Rb/Sr and Sr isotopic signatures of different white mica fractions as potentially containing relevant age information on the crystallization history of the rocks. The alternative possibility that the spread in white mica signatures simply reflect mixing between high-Rb/Sr phengite and low-Rb/Sr inclusions is discarded because of the following three arguments:

- First, small inclusions have been efficiently removed by the purification procedures so that they cannot cause the observed Sr concentration variability. Variable K/Ca ratios derived from the Ar isotope analyses indicate the presence of small inclusions in white mica, but the preparation

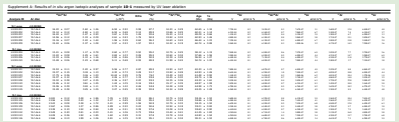

[1]Supplemental File. Complete set of Ar isotopic data. Please visit https://doi.org/10.1130/GES01521.S1 or the full-text article on www.gsapubs.org to view the Supplemental File.

TABLE 3. IN SITU $^{40}Ar/^{39}Ar$ DATES, SESIA ZONE SAMPLES (WESTERN ALPS, ITALY)

Analysis ID	Disc	Age (Ma)		1σ (m.y.)
10-1 cores				
U1301201	Ar-4	64.65	±	1.34
U1301202	Ar-4	62.21	±	1.14
U1301203	Ar-4	69.09	±	0.66
U1301207	Ar-4	62.93	±	1.46
U1301208	Ar-4	66.44	±	1.03
U1301209	Ar-4	64.74	±	0.88
U1301101	Ar-6	63.30	±	1.21
U1301102	Ar-6	62.93	±	1.26
U1301103	Ar-6	61.48	±	0.92
U1301107	Ar-6	65.75	±	1.36
U1301108	Ar-6	65.30	±	1.61
U1301110	Ar-6	68.97	±	1.59
U1301114	Ar-6	64.98	±	1.73
U1301115	Ar-6	65.25	±	1.28
Average		**64.86**		
Standard Deviation		**2.27**		
10-1 rims				
U1301204	Ar-4	58.12	±	1.15
U1301205	Ar-4	57.66	±	1.56
U1301206	Ar-4	56.54	±	1.27
U1301210	Ar-4	54.74	±	1.00
U1301104	Ar-6	58.16	±	1.53
U1301105	Ar-6	58.86	±	1.08
U1301106	Ar-6	58.15	±	1.52
U1301109	Ar-6	59.01	±	0.82
U1301111	Ar-6	59.63	±	0.90
U1301112	Ar-6	61.25	±	1.83
U1301113	Ar-6	62.80	±	1.54
U1301116	Ar-6	59.31	±	1.53
Average		**58.69**		
Standard Deviation		**2.07**		
MK-54 cores				
U1300701	Ar-5	59.74	±	0.58
U1300702	Ar-5	64.96	±	0.58
U1300703	Ar-5	67.22	±	1.14
U1300704	Ar-5	59.53	±	0.96
U1300709	Ar-5	58.97	±	1.25
U1300710	Ar-5	59.99	±	0.62
U1300711	Ar-5	60.36	±	1.31
U1300712	Ar-5	59.82	±	1.46
U1300717	Ar-5	59.24	±	1.29
U1300801	Ar-1	61.54	±	1.30
U1300802	Ar-1	58.34	±	0.76
U1300803	Ar-1	58.61	±	0.88
U1300808	Ar-1	62.54	±	1.15

(*continued*)

TABLE 3. IN SITU $^{40}Ar/^{39}Ar$ DATES, SESIA ZONE SAMPLES (WESTERN ALPS, ITALY) (*continued*)

Analysis ID	Disc	Age (Ma)		1σ (m.y.)
MK-54 cores (*continued*)				
U1300810	Ar-1	61.51	±	1.13
U1300811	Ar-1	61.93	±	1.51
U1300901	Ar-3	61.49	±	0.94
U1300902	Ar-3	61.32	±	0.76
U1300905	Ar-3	59.81	±	0.99
Average		**60.94**		
Standard Deviation		**2.25**		
MK-54 rims				
U1300705	Ar-5	54.04	±	1.20
U1300706	Ar-5	39.22	±	2.80
U1300707	Ar-5	57.68	±	0.90
U1300708	Ar-5	40.03	±	2.32
U1300713	Ar-5	37.78	±	1.29
U1300714	Ar-5	32.79	±	1.03
U1300715	Ar-5	34.59	±	1.51
U1300716	Ar-5	43.34	±	1.52
U1300718	Ar-5	43.46	±	0.89
U1300804	Ar-1	34.01	±	0.58
U1300805	Ar-1	38.90	±	1.77
U1300806	Ar-1	44.34	±	1.66
U1300807	Ar-1	51.37	±	1.14
U1300809	Ar-1	51.67	±	1.17
U1300812	Ar-1	46.94	±	1.44
U1300903	Ar-3	46.54	±	1.92
U1300904	Ar-3	51.93	±	1.51
U1300906	Ar-3	41.86	±	1.87
Average		**43.92**		
Standard Deviation		**7.28**		
3i cores				
U1300501	Ar-4p	71.48	±	2.97
U1300502	Ar-4p	80.23	±	2.16
U1300503	Ar-4p	76.45	±	1.63
U1300509	Ar-4p	76.42	±	0.81
U1300510	Ar-4p	75.44	±	0.60
U1301004	Ar-4	75.11	±	0.79
U1301005	Ar-4	72.80	±	1.29
U1301006	Ar-4	75.85	±	0.90
U1301010	Ar-4	75.52	±	1.48
U1301011	Ar-4	75.75	±	1.36
U1301012	Ar-4	79.18	±	0.93
U1301013	Ar-4	75.45	±	1.22
U1301014	Ar-4	76.14	±	1.12
U1300602	Ar-6	64.43	±	1.93
U1300603	Ar-6	69.68	±	1.43

(*continued*)

TABLE 3. IN SITU $^{40}Ar/^{39}Ar$ DATES, SESIA ZONE SAMPLES (WESTERN ALPS, ITALY) (*continued*)

Analysis ID	Disc	Age (Ma)		1σ (m.y.)
3i cores (*continued*)				
U1300605	Ar-6	74.48	±	0.96
U1300607	Ar-6	75.46	±	2.19
U1300609	Ar-6	76.50	±	1.66
U1300611	Ar-6	74.11	±	1.14
U1300613	Ar-6	77.62	±	1.22
U1300615	Ar-6	76.28	±	0.85
U1300616	Ar-6	72.11	±	1.45
U1300617	Ar-6	72.45	±	1.10
U1300619	Ar-6	82.27	±	1.83
U1300622	Ar-6	80.61	±	1.19
U1300624	Ar-6	78.24	±	1.52
Average		**75.39**		
Standard Deviation		**3.62**		
3i rims				
U1301001	Ar-4	61.02	±	1.52
U1301002	Ar-4	62.37	±	1.07
U1301003	Ar-4	63.50	±	1.26
U1301007	Ar-4	66.17	±	2.64
U1301008	Ar-4	60.21	±	1.71
U1301009	Ar-4	59.93	±	1.26
U1301015	Ar-4	62.33	±	1.50
U1301016	Ar-4	64.94	±	1.30
U1300601	Ar-6	67.97	±	2.87
U1300604	Ar-6	61.62	±	1.57
U1300606	Ar-6	60.16	±	0.97
U1300608	Ar-6	65.38	±	1.04
U1300610	Ar-6	56.79	±	2.02
U1300612	Ar-6	57.44	±	2.04
U1300614	Ar-6	58.43	±	1.55
U1300618	Ar-6	60.99	±	1.37
U1300620	Ar-6	68.74	±	1.19
U1300621	Ar-6	58.95	±	0.82
U1300623	Ar-6	68.44	±	1.39
Average		**62.39**		
Standard Deviation		**3.67**		
MK99				
U0702301	f	82.58	±	0.88
U0702302	f	82.08	±	2.39
U0702303	f	87.67	±	1.17
U0702304	f	85.89	±	1.13
U0702305	f	86.27	±	4.10
U0702306	f	89.16	±	1.09
U0702307	f	111.09	±	7.06
U0702308	f	83.70	±	1.07

(*continued*)

TABLE 3. IN SITU $^{40}Ar/^{39}Ar$ DATES, SESIA ZONE SAMPLES (WESTERN ALPS, ITALY) (*continued*)

Analysis ID	Disc	Age (Ma)		1σ (m.y.)
MK99 (*continued*)				
U0702309	f	87.07	±	0.61
U0702310	f	89.95	±	0.66
U0702311	f	88.34	±	0.69
U0703101	DS	92.85	±	1.07
U0703102	DS	86.71	±	1.52
U0703103	DS	81.86	±	0.55
U0703106	DS	88.97	±	0.79
U0703107	DS	89.90	±	0.69
U0703108	DS	83.71	±	1.82
U0703109	DS	99.71	±	5.88
U0703110	DS	89.21	±	10.90
Average		**88.77**		
Standard Deviation		**6.84**		

procedures drastically reduce the amount of inclusions: All brittle inclusions bigger than the thickness of the mica flakes, ~10 mm, would have been released by the grinding procedure and eliminated from the phengite fraction, and most of the inclusions smaller than that would have also been washed away. For four of the five samples analyzed (MK-99, MK-118, MK-174, and 3i), one would need several weight percent of Sr-rich apatite or epidote inclusions in mica to generate the observed effects, which can be ruled out. There is only sample (MK-161) with extremely high Sr contents in epidote so that small amounts of epidote inclusions could account for the range in Sr concentrations observed in white mica.

- Second, the systematic correlation between grain size and Rb/Sr of the mica fraction, observed in all samples where distinct sets of age information can be extracted (samples MK-174, MK-161 and 3i), would not occur due to random incorporation of inclusions. Hence, the concept of inclusion-controlled variability of Rb/Sr ratios does not explain the commonly observed correlation between mica grain size and chemical signature as expressed in terms of Sr concentration in this case.
- Third, if differences between the different white mica grain size fractions were caused by inclusions of epidote or apatite, a regression line through the mica fractions would pass through the focal point of those inclusions. This is not the case for two of the samples that provide heterogeneous age information due to grain size dependency of apparent mica ages (samples MK-174 and 3i). For both, the regression lines through the mica fractions alone intersect the $^{87}Sr/^{86}Sr$ axis above the initial $^{87}Sr/^{86}Sr$ values derived from the regression line for all mineral data including apatite and epidote (sample MK-174: 0.7155 versus 0.7128; sample 3i: 0.71073 versus 0.71046), and hence the variability in

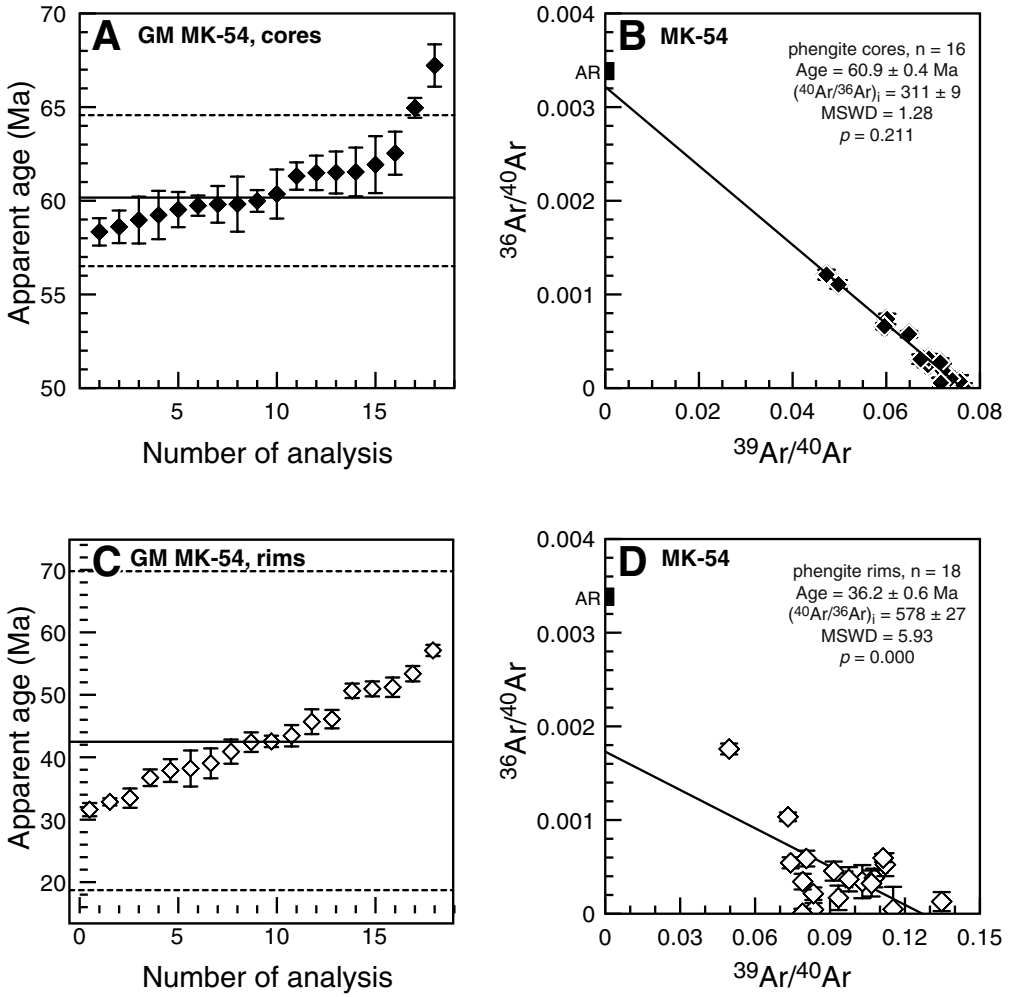

Figure 7. Phengite $^{40}Ar/^{39}Ar$ age frequency distribution diagrams and inverse isochron diagrams of the greenschist-facies mylonite from the Tallorno shear zone (sample MK-54), subdivided into relict cores (A, B) and overprinted rims (C, D). Median values (black lines) and limits for the definition of outliers (stippled lines) are shown in the frequency distribution diagrams. Limits for outliers are defined based on the interquartile range (IQR) as upper quartile (Q3) + 1.5 IQR and lower quartile (Q1) – 1.5 IQR. Outliers are not considered for the calculation of the inverse isochron. $(^{40}Ar/^{36}Ar)_i$ is the initial $^{40}Ar/^{36}Ar$ isotopic ratio derived from the inverse isochron. Short black bars labeled AR in panels B and D indicate the atmospheric $^{36}Ar/^{40}Ar$ ratio. GM—*gneiss minuti*; MSWD—mean square weighted deviation.

$^{87}Rb/^{86}Sr$ ratios of the different mica grain size fractions cannot be solely explained by inclusions.

Interpretation of Rb-Sr Internal Mineral Isochron Data

The two blueschist-facies mylonites (samples MK-99 and MK-118; Figs. 5A, 5B) show no obvious correlation between white mica grain size and apparent ages for the respective fractions. Therefore, a near-complete isotopic re-equilibration of the white mica population during deformation is assumed. The strong foliation and the alignment of all major mineral phases, including phengite (Fig. 4A), argue for synkinematic recrystallization in the blueschist-facies mylonites. Synkinematic recrystallization in mylonites generally causes Sr isotopic re-equilibration between mica and coexisting phases at temperatures as low as 300 °C (Müller et al., 1999) and hence provides constraints on mica recrystallization during deformation (Freeman et al., 1998; Bröcker and Franz, 2005; Glodny et al., 2008a). Moreover, thermally induced resetting of the Rb-Sr system in white micas requires temperatures in excess of 550–600 °C (Inger and

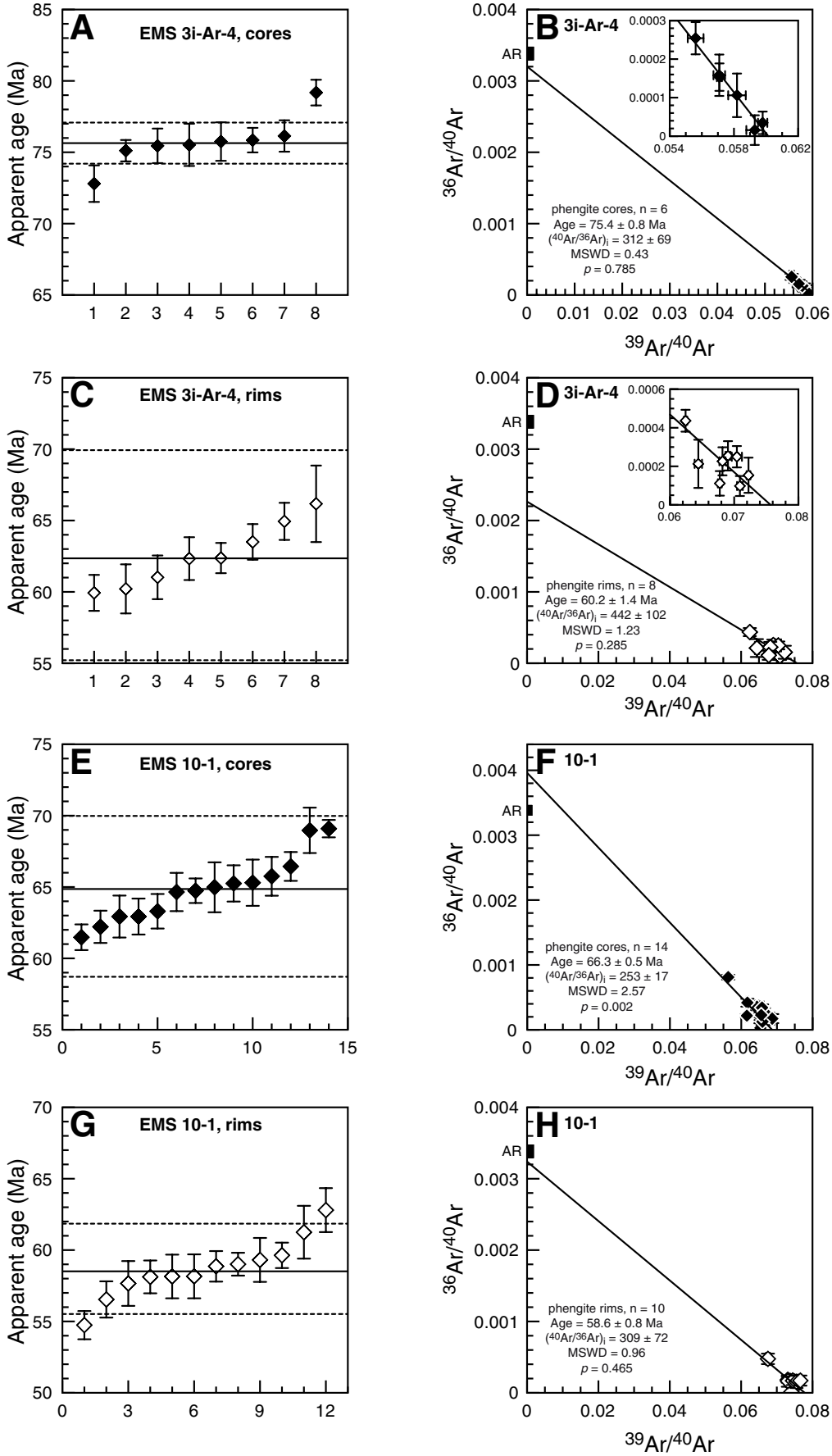

Figure 8. Phengite $^{40}Ar/^{39}Ar$ age frequency distribution diagrams and inverse isochron diagrams of micaschists from the eclogitic micaschists (EMS) unit. Median values (black lines) and limits for the definition of outliers (stippled lines) are shown in the frequency distribution diagrams. Limits for outliers are defined based on the interquartile range (IQR) as upper quartile (Q3) + 1.5 IQR and lower quartile (Q1) – 1.5 IQR. Outliers are not considered for the calculation of the inverse isochrons. (A–D) Cores (A, B) and overprinted rims (C, D) of disc Ar-4 from sample 3i. (E–H) Cores (E, F) and overprinted rims (G, H) of sample 10-1. $(^{40}Ar/^{36}Ar)_i$ is the initial $^{40}Ar/^{36}Ar$ isotopic ratio derived from the inverse isochron. Short black bars labeled AR in the inverse isochron diagrams indicate the atmospheric $^{36}Ar/^{40}Ar$ ratio. MSWD—mean square weighted deviation.

Cliff, 1994; Villa, 1998; Glodny et al., 2008b), and these temperatures were not reached during the blueschist-facies recrystallization of these mylonites.

In more weakly deformed rocks, mixed white mica populations and Sr isotopic inhomogeneities can be identified by analyzing different grain size fractions in white mica. Isotopic inhomogeneities are the reflection of unequilibrated relict grains or incomplete recrystallization, and they may render the age information geologically meaningless or at least difficult to interpret (Freeman et al., 1998; Müller et al., 1999). We observe a positive correlation between white mica grain size and apparent age in three samples (MK-174, MK-161, and 3i; Figs. 5C–5F). This correlation suggests either a prolonged deformation-induced recrystallization process (i.e., the older white mica grains crystallized during the early deformation stages) or partial isotopic inheritance from the precursor rocks (Angiboust et al., 2014, 2016). Distinct origins of the phengite populations are also indicated by the highly variable phengite grain sizes in the eclogitic micaschists (EMS). Large mica flakes (>500 µm), commonly oblique to the main foliation, occur together with more strongly aligned, smaller, and more elongated phengite (Figs. 4C, 4D). Evidence for Sr isotopic inhomogeneities in the greenschist-facies mylonite (sample MK-174) and both EMS samples (samples MK-161 and 3i) is also indicated by distinct $^{87}Sr/^{86}Sr$ ratios of the low-Rb/Sr phases (Table 2; Fig. 5). These differences are attributed to incomplete isotopic resetting during the different episodes of recrystallization. By combining the large-grain-size white mica fraction with low-Rb/Sr minerals that have not fully re-equilibrated, we obtained minimum ages for the relict assemblages.

Incomplete reactivity of matrix minerals (Sousa et al., 2013) may cause Sr incorporated into a recrystallizing phengite to have a very different isotopic composition from the Sr in the low-Rb/Sr minerals analyzed. We tried to control this effect by combining, where feasible, Rb-Sr data for low-Rb/Sr minerals with low shear strength and high Sr diffusivities with Rb-Sr data for fine-grained, recrystallized phengite to calculate age estimates for ductile deformation. These phases are most likely to participate in the dynamic processes of recrystallization, fluid-rock interaction, and isotopic re-equilibration during deformation. For instance, in EMS sample 3i, epidote may have remained a closed system during deformation, but the Sr signature of calcite is assumed to be a good proxy for the Sr signature available for incorporation into recrystallizing phengite. Shear strength for calcite is low at mid-crustal conditions, considerably lower than that of quartz (Dresen et al., 1998), and diffusion of Sr in calcite is comparatively rapid (Cherniak, 1997). We therefore assume that for sample 3i, the age estimate from calcite and fine-grained phengite is the best approximation of the age of ductile shearing causing phengite recrystallization. In other samples (MK-174, MK-161), apatite and fine-grained phengite were combined to derive age estimates for late stages of deformation. Apatite also recrystallizes comparatively easily and is hence likely to represent an open system ready to exchange Sr with contemporaneously recrystallizing phengite under conditions of mid-crustal deformation.

Semiquantitative estimates of the whole-rock Rb-Sr signatures, based on mineral modes (Table 1) and Rb-Sr signatures of the minerals (Table 2), suggest that the observed differences in initial $^{87}Sr/^{86}Sr$ ratios for the low-Rb/Sr phases are compatible with in situ radiogenic ingrowth. No metasomatic additions of Sr are required. Considering a time gap of 15 m.y. between initial crystallization and re-equilibration, reflecting radiogenic ingrowth from 75 to 60 Ma, the $^{87}Sr/^{86}Sr$ ratio of sample 3i would change from 0.7103 to 0.7106. For sample MK-161, $^{87}Sr/^{86}Sr$ would increase from 0.731 to 0.738. Both changes are consistent with the observed variability in low-Rb/Sr phases considering the uncertainties in modal mineral proportions and exact timing and completeness of equilibration.

$^{40}Ar/^{39}Ar$ Inverse Isochrons

Inverse isochron diagrams that combine several in situ $^{40}Ar/^{39}Ar$ analyses from texturally identical areas in different mineral grains within a sample can provide reliable age information for distinct stages of mineral growth (Halama et al., 2014). Here, we observe a clear distinction in ages between relict phengite cores and overprinted areas. Different samples from within the EMS unit as well as in comparison to the *gneiss minuti* (GM) unit show distinct age distributions for core and overprinted rims (Figs. 7 and 8). Moreover, inverse isochron diagrams can be used to evaluate effects of Ar loss and/or excess ^{40}Ar ($^{40}Ar_E$) incorporation (Kuiper, 2002). Loss of Ar from the mineral causes a shift of the data points toward higher $^{39}Ar/^{40}Ar$ ratios because ^{39}Ar is produced from ^{39}K during irradiation and not affected by this process. Argon loss results in younger apparent $^{40}Ar/^{39}Ar$ ages and, if incomplete, produces inverse isochron ages between the formation age and the time when Ar loss stopped (Kuiper, 2002). Excess ^{40}Ar can be generated in closed, fluid-poor systems, where radiogenic Ar produced by relict K-bearing phases is not removed (Kelley, 2002; Warren et al., 2012b). Trapping of $^{40}Ar_E$ in the mineral results in coupled isotope ratio variations along both axes in the inverse isochron diagram, but the displacement toward lower $^{36}Ar/^{40}Ar$ ratios is quite characteristic for this process (Kuiper, 2002). In this study, we use several criteria to evaluate the significance of the $^{40}Ar/^{39}Ar$ dates. A relatively small scatter in individual $^{40}Ar/^{39}Ar$ dates combined with a statistically reliable inverse isochron and a $(^{40}Ar/^{36}Ar)_i$ ratio (the initial $^{40}Ar/^{36}Ar$ ratio at the intercept with the y-axis) overlapping the atmospheric ratio are taken to reflect a single age of a recrystallization event (e.g., relict cores of sample section 3i-Ar-4, Figs. 8A, 8B). In contrast, a large spread of individual $^{40}Ar/^{39}Ar$ dates combined with an inverse isochron that shows a low statistical reliability and no overlap of $(^{40}Ar/^{36}Ar)_i$ with the atmospheric ratio is interpreted to represent a near-continuous sequence of individual recrystallization ages (e.g., overprinted rims of sample MK-54, Figs. 7C, 7D).

Mobility and Exchange of Radiogenic Isotopes

The investigated metamorphic rocks from the Sesia zone provide a useful case study to assess the principal factors controlling the isotope record and

to evaluate the significance of the ages recorded. The two opposing models to be discussed are fluid-assisted recrystallization, which involves mineral replacement reactions via dissolution and reprecipitation of phases (Putnis, 2009; Villa, 2016), versus temperature-controlled diffusion (e.g., Harrison et al., 2009; Baxter, 2010).

The petrological evidence provides some of the strongest arguments in support of the important role of dissolution-reprecipitation mechanisms for isotopic equilibration in the Sesia zone rocks. The steep compositional gradients observed in phengite and glaucophane in samples of this study (Fig. 4) evidence petrologic disequilibrium and demonstrate the necessity for fast, fluid-assisted element transport to have occurred (Konrad-Schmolke et al., 2011a). In rocks where petrologic disequilibrium evidently persists, diffusive re-equilibration was demonstrably absent (Villa, 2010), and hence diffusion in these rocks of all elements defining the petrologic disequilibria was irrelevant during and after the establishment of the disequilibrium paragenesis.

Distinct $^{40}Ar/^{39}Ar$ age domains in phengite (Figs. 6–8) demonstrate Ar isotopic disequilibrium. Differences in apparent $^{40}Ar/^{39}Ar$ ages are on the order of several million years (Table 3). The distinct age domains coincide with differences in mineral chemistry that reflect fluid-triggered compositional modifications (Halama et al., 2014). The presence of isotopic zoning is interpreted to be predominantly controlled by growth zoning during mineral dissolution-reprecipitation reactions compared to diffusion (Villa, 2016). Moreover, thermal diffusion of Ar in white mica is inefficient for the low-*T* high-*P* eclogite-facies conditions experienced by the Sesia zone rocks (Putlitz et al., 2005; Warren et al., 2012a). Hence $^{40}Ar/^{39}Ar$ ages record crystallization and recrystallization ages rather than cooling ages below the Ar closure temperature.

For the Rb-Sr system, it is significant that we can observe and isotopically distinguish two sub-parageneses by constructing distinct internal Rb-Sr isochrons from a single sample (Fig. 5). The distinct ages and isotopic signatures suggest that deformation and metamorphic recrystallization control the isotopic signatures. In summary, constraints from petrology, $^{40}Ar/^{39}Ar$ in situ data, and Rb-Sr data all point to the dominant role of fluid-induced recrystallization in determining the geochronological information observed.

Age Significance and Isotope Mobility

Blueschist-Facies Mylonites

The Nantay shear zone (NSZ) and Tallorno shear zone (TSZ) separate the EMS from the GM and show a mylonitic foliation. They are interpreted as thrust zones along which the eclogite-facies rocks of the EMS were juxtaposed against the GM (Giuntoli and Engi, 2016). The oriented crystallization of glaucophane, phengite, and epidote parallel to the foliation (Fig. 3B) points to co-recrystallization during deformation and demonstrates that the deformation began under blueschist-facies conditions. The age of this deformation stage is given as 60.1 ± 0.9 Ma by a Rb-Sr isochron that includes all three of these minerals (sample MK-118; Fig. 5A). All different white mica fractions plot on the same isochron. This blueschist-facies deformation age had not been well established before, and it is supported by a second Rb-Sr isochron yielding 60.9 ± 2.1 Ma (sample MK-99; Fig. 5B). Some small disequilibria among the different white mica populations in this sample might be related to incomplete isotopic equilibration of preexisting phengites during deformation (Cliff et al., 2017). Elevated MSWD (Wendt and Carl, 1991) values for both blueschist-facies mylonites (Figs. 3A, 3B) suggest scatter in excess of experimental uncertainties. For mylonite MK-118, this is due to small disequilibria between the low-Rb/Sr phases. In the case of mylonite MK-99, some scatter may be caused by mechanical rotation of older phengite grains into new deformation fabrics, leading to the mixing of different mica generations and the preservation of older isotopic signatures (Bröcker et al., 2013; Cliff et al., 2017). However, the MSWD values alone cannot distinguish between useful and useless age information because MSWD is also a function of the analytical precision of the data (Kalsbeek and Hansen, 1989). The degree of initial disequilibrium is almost negligible compared to the radiogenic ^{87}Sr ingrowth in the mica, pointing to near-complete equilibration in both samples during blueschist-facies recrystallization.

In contrast to the Rb-Sr age of 60.9 ± 2.1 Ma from sample MK-99, the in situ apparent $^{40}Ar/^{39}Ar$ ages from the same sample span a range of ~30 m.y. from ca. 111 to ca. 82 Ma (Table 3). Given the well-defined structural position of this sample in a major shear zone (Fig. 1) and the geochemical evidence for fluid-rock interaction (Halama et al., 2014), the differential behavior between the Rb-Sr and $^{40}Ar/^{39}Ar$ systems is enigmatic. The Ar system in sample MK-99 did not re-equilibrate during deformation at ca. 60 Ma, based on the lack of in situ apparent $^{40}Ar/^{39}Ar$ ages <80 Ma, whereas the Rb-Sr system did. Cases where Rb-Sr white mica ages are younger than corresponding $^{40}Ar/^{39}Ar$ ages have also been described from metamorphic rocks in the Greek Cyclades (Altherr et al., 1979; Bröcker and Franz, 1998). These observations can be explained by disturbance of Ar retention by multiple episodes of recrystallization or the presence of excess ^{40}Ar ($^{40}Ar_E$), where radiogenic ^{40}Ar was introduced from outside the system and incorporated into the mineral during crystallization (Bröcker and Franz, 1998; Kelley, 2002; Sherlock and Kelley, 2002). Metamorphic fluids, which typically exhibit an excess of ^{40}Ar, can be trapped in micropores during ductile deformation (Cumbest et al., 1994) or incorporated as fluid inclusions (Kelley, 2002). If fluids circulating through shear zones have previously interacted with ancient basement rocks and contain high concentrations of radiogenic ^{40}Ar, significant quantities of $^{40}Ar_E$ would partition into minerals (Cumbest et al., 1994). The incorporation of radiogenic ^{40}Ar into recrystallizing phengite from ambient fluids would be heterogeneous and would bear no relation to a specific age. Due to the increase in phengite-fluid partition coefficients for Ar with pressure, $^{40}Ar_E$ from aqueous fluids may preferentially accumulate in phengites under high-pressure to ultrahigh-pressure conditions (Menold et al., 2016). The comparison between the $^{40}Ar/^{39}Ar$ and Rb-Sr systems reveals that equilibration of the Rb-Sr system during deformation does not

necessarily imply equilibration of the K-Ar system with complete loss of radiogenic Ar from the system as well.

Greenschist-Facies Mylonites

The TSZ is in a structurally similar position to the NSZ, juxtaposing the EMS against the GM. The two mylonites from the TSZ (samples MK-54 and MK-174) have a greenschist-facies metamorphic foliation and lack a syn-kinematic blueschist-facies mineralogy, although pseudomorphs after sodic amphibole indicate an earlier blueschist-facies equilibration.

The Sr isotope disequilibria in the greenschist-facies mylonites (sample MK-174) preserve evidence for an early, pre–greenschist facies history with recrystallization older than 55.7 ± 0.8 Ma based on Rb-Sr signatures of allanite and white mica >250 μm (Fig. 5C). The old, possibly relict, coarse white mica crystals are isotopically and chemically different from the apparently younger, finer white mica crystals. The finer the white mica is, the lower is its Sr content, the higher the $^{87}Rb/^{86}Sr$ ratio, and the lower it plots relative to the regression line for all data in an isochron diagram (Fig. 5C). In other words, the finer grained the white mica is, the lower is the apparent age that can be calculated for the respective mica fraction. The fine white mica is related to the late increments of greenschist-facies overprinting and recrystallization, which occurred at or shortly after 46.5 ± 0.7 Ma. This implies that local reactivation and recrystallization along the TSZ under greenschist-facies conditions continued at least until this time.

Phengitic white mica in the greenschist-facies mylonite (sample MK-54) shows a clear distinction between in situ core and rim $^{40}Ar/^{39}Ar$ ages (Fig. 6B). Two relict cores with older ages of ca. 65 and ca. 67 Ma are outliers indicative of excess ^{40}Ar incorporation (Fig. 7A). The $^{40}Ar/^{39}Ar$ inverse isochron age of 60.9 ± 0.4 Ma (Fig. 7B) overlaps Rb-Sr isochron ages from blueschist-facies mylonites. The wide scatter in apparent $^{40}Ar/^{39}Ar$ ages for the overprinted rims covers a range of ~25 m.y. (Fig. 7c). This large spread can be attributed to continuous or repeated recrystallization and/or resetting, as observed in metamorphic rocks of the Attic-Cycladic belt (Greece) (Bröcker et al., 2013) and the Sanbagawa belt (southwestern Japan) (Itaya et al., 2011). Late increments of retrograde overprinting and recrystallization occurred at least until 46.5 ± 0.7 Ma based on the Rb-Sr data (Fig. 5C), but later phases of deformation and recrystallization are indicated by Rb-Sr isochron ages of ca. 38–40 Ma (recalculated using the new ^{87}Rb decay constant) from the GM (Inger et al., 1996). Along these lines, the apparent $^{40}Ar/^{39}Ar$ ages of 58–33 Ma are interpreted to record continuous or repeated retrograde recrystallization in the greenschist facies. Fluid-mediated recrystallization and re-equilibration is to be expected during greenschist-facies metamorphism because fluid ingress during exhumation through the greenschist facies is a very common phenomenon (Proyer, 2003; Villa, 2010). Moreover, water saturation during decompression from blueschist to greenschist facies can be attained without external water influx, as decompression along the retrograde *P-T* path may result in dehydration because the capability of the rock to retain water diminishes (Halama and Konrad-Schmolke, 2015). Calc-alkaline dikes of andesitic and basaltic composition, which are probably related to emplacement of Periadriatic plutons at ca. 33 Ma (Berger et al., 2012), postdate the greenschist-facies foliation (Giuntoli and Engi, 2016) and mark the end of deformation and recrystallization in the GM.

Similarly to the blueschist-facies mylonites, the Ar isotope system records an early phase of re-equilibration in the greenschist-facies part of the shear zone, whereas the Rb-Sr system preserves evidence of later re-equilibration even though it did not fully equilibrate, and provides at least a maximum age for the end of ductile deformation-related recrystallization under greenschist-facies conditions. Movement along the major shear zones between the EMS and GM units within the Sesia zone continued for at least ~15 m.y. based on published $^{40}Ar/^{39}Ar$ data (65.0 ± 3.0 Ma for mylonitic phengite; Halama et al., 2014) and the new Rb-Sr age for late increments of deformation (46.5 ± 0.7 Ma for a greenschist-facies mylonite). Deformation ages are not homogeneous along the shear zone, but vary depending on whether they reflect blueschist- or greenschist-facies conditions.

Eclogitic Micaschists (EMS)

Eclogite-facies fluid-induced recrystallization. The eclogitic microlithons (Fig. 6A) in sample MK-161 presumably reflect the oldest recrystallization episodes during high-pressure metamorphism in that sample. However, some influence of the deformation and shearing is already recognizable in the eclogitic microlithons based on the observed Sr isotope disequilibria. The small differences in the Sr isotopic composition of the two omphacites could be related to different degrees of retrograde overprint or to different initial isotope compositions of the two omphacite clusters (Table 2). The age of 72.4 ± 1.1 Ma, which is based on E-omp1 and E-wm3 (Fig. 5D), is slightly higher than the one based on all data points and constrains the minimum age of the eclogite-facies recrystallization. Similar constraints for the minimum age of the eclogite-facies recrystallization are derived from the sheared matrix of sample MK-161 (Fig. 6A), where coarse-grained white mica and epidote yield an age of 77.2 ± 0.8 Ma (Fig. 5E). The large white mica grains in the matrix are relatively enriched in Sr, resulting in lower $^{87}Rb/^{86}Sr$ ratios, and they appear significantly older than the smaller grains (160–250 μm) in the foliation. These minimum ages overlap $^{40}Ar/^{39}Ar$ inverse isochron ages of phengite cores in micaschist sample 3i, which range from 74.6 ± 0.7 to 75.8 ± 0.9 (Halama et al., 2014), including the new age of 75.4 ± 0.8 Ma (Fig. 8B). This recrystallization event is not related to any large-scale deformation structures, as the samples derive from several kilometers away from the shear zone and mylonites of this age are lacking. Instead, the ages are interpreted to reflect fluid-rock interaction and associated recrystallization. Both the minimum ages for relict assemblages in the Rb-Sr system and the in situ $^{40}Ar/^{39}Ar$ phengite core ages reflect this process (Fig. 9). Our interpretation of a significant episode of fluid-induced, eclogite-facies

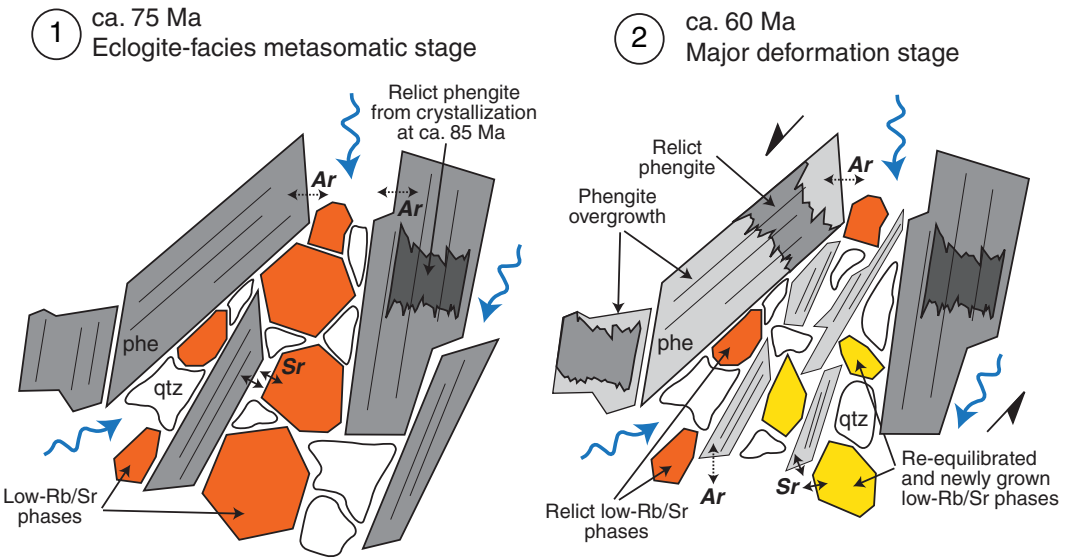

Figure 9. Idealized sketch illustrating recrystallization and equilibration and of the Ar and Sr isotope systems in the eclogitic micaschists (EMS) based on the samples investigated in this study. At the eclogite-facies metasomatic stage (1), both Ar and Sr equilibrate with the grain boundary fluid (blue arrows). Relict phengite (phe) cores from an earlier high-pressure crystallization stage at ca. 85 Ma (dark gray) may be preserved (Halama et al., 2014). During the deformation stage (2), major strain is focused in the adjacent shear zones (black half-arrows), but recrystallization in the EMS causes re-equilibration of Ar and Sr in phengite overgrowths and newly grown, small phengite (light gray) with the grain boundary fluid, whereas relict phengite grains (medium gray) retain information about preceding crystallization events. Relict low-Rb/Sr phases (orange) preserve the Sr isotopic information of prior equilibration, whereas some low-Rb/Sr phases (yellow) grow anew or re-equilibrate. These features allow the determination of distinct $^{40}Ar/^{39}Ar$ phengite core and rim ages and the calculation of two distinct Rb-Sr ages from one sample, reflecting a minimum age of the previous recrystallization and maximum age of deformation, respectively. qtz—quartz.

recrystallization in the EMS unit at ca. 75 Ma is in line with the observation of dispersed fluid flow and repeated fluid-rock interaction being responsible for hydration in the Sesia zone (Giuntoli et al., 2018a) and a U-Pb zircon age of 76 ± 1 Ma from a metamorphic vein that was related to fluid influx (Rubatto et al., 1999). The relevance of this age for high-pressure fluid-induced recrystallization in the EMS unit is emphasized by similar ages obtained in zircon rims by U-Pb (74.6 ± 2.1 Ma; Regis et al., 2014) and in phengite by $^{40}Ar/^{39}Ar$ plateau ages (73.6 ± 0.3 to 76.9 ± 0.6 Ma; Ruffet et al., 1995) and in situ $^{40}Ar/^{39}Ar$ data (74–77 Ma; Halama et al., 2014).

Of the low-Rb/Sr phases in sample 3i, apatite has the lowest $^{87}Sr/^{86}Sr$ ratio (0.71033). Apatite + coarse white mica (>1000 μm) are considered as a relict assemblage and yield an apparent age of 64.5 ± 1.5 Ma, which is interpreted as a minimum age for a preceding metamorphic recrystallization episode. An overlapping $^{40}Ar/^{39}Ar$ age of 66.3 ± 0.5 Ma is observed in the relict phengite cores of sample 10-1 (Fig. 8F). This suggests that these relict cores (Fig. 6D) reflect the same event as the Rb-Sr age, indicating that the resetting of the Rb-Sr age is quite small. Sample 10-1 is very close to the TSZ, so that any eclogite-facies history has been completely obliterated by metasomatic recrystallization and therefore no older ages are recorded in this sample.

Deformation-induced recrystallization. The white mica population in the sheared matrix of sample MK-161 (Figs. 3F, 5E) reflects distinct phases of equilibration, as evident in the positive correlation between white mica grain size and apparent ages. The low-Rb/Sr phases are also in disequilibrium. The Sr isotopic ratios of the low-Rb/Sr eclogite-facies minerals epidote (0.7309) and omphacite (0.7270–0.7281) and the initial $^{87}Sr/^{86}Sr$ derived from the relict assemblage regression line in the matrix (0.7309) are clearly distinct from the initial $^{87}Sr/^{86}Sr$ derived from the deformation assemblage regression line (0.7363). Epidote has the lowest $^{87}Sr/^{86}Sr$ ratio, suggesting that it is the oldest of the low-Rb/Sr phases present, as re-equilibration at a later stage would invariably have caused an increase in the $^{87}Sr/^{86}Sr$ ratio of the whole rock because it is a Rb-rich system. The other low-Rb/Sr phases titanite and apatite have higher $^{87}Sr/^{86}Sr$ ratios than epidote, indicating that they interacted with the surrounding matrix at a later stage. The deformation assemblage of fine-grained white mica, apatite, and titanite yields a Rb-Sr age of 60.1 ± 1.1 Ma, representing a maximum age for the end of deformation (cf. Angiboust et al., 2014).

The Sr isotopic disequilibria between the different white mica populations in micaschist 3i are smaller than those in sample MK-161, but the general pattern with apparently higher ages for larger white mica crystals and lower ages for the finer populations is similar (Fig. 5F). Selecting calcite + fine white mica (250–160 μm) as the deformation assemblage, the age of 58.1 ± 1.1 Ma is interpreted as maximum age for the end of the deformation-induced recrystallization.

Further support for an isotopic resetting in the EMS related to deformation in the TSZ comes from the $^{40}Ar/^{39}Ar$ inverse isochron ages of the overprinted rims in micaschist samples 3i and 10-1, with ages of 60.2 ± 1.4 Ma (Fig. 8D) and 58.6 ± 0.8 Ma (Fig. 8H), respectively. The initial $^{40}Ar/^{36}Ar$ for the overprinted rims in sample 3i is higher than the atmospheric ratio and poorly defined (Fig. 8D), which is likely due to the presence of excess ^{40}Ar, possibly augmented by the uncertainty in the initial $^{40}Ar/^{36}Ar$ ratio due to the concentration of data points close to the *x*-axis.

The two Rb-Sr ages of the deformation assemblages (60.1 ± 1.1 Ma in sample MK-161, and 58.1 ± 1.1 Ma in sample 3i), recorded in samples that are 4.5 km away from each other, and the in situ $^{40}Ar/^{39}Ar$ phengite rim data provide the same geochronological information (Fig. 9). Both are in good agreement with the two Rb-Sr isochrons from the mylonites of the NSZ. Hence, they are interpreted to reflect late increments of ductile deformation and fluid-induced recrystallization in the EMS and are probably very close to the true age of these increments. Even though the EMS samples are relatively weakly deformed compared to the mylonites from the major shear zones, syn-kinematic fluid flow within the EMS must have propagated into the surrounding rocks over distances of several kilometers to cause the observed Sr isotopic resetting. A similar observation was made based on garnet textures in the Sesia zone by Giuntoli et al. (2018a).

Age Distribution in the Sesia Zone

Based on the new data, data previously published in an accompanying study (Halama et al., 2014), and abundant geochronological data from the literature, several distinct episodes of crystallization and re-crystallization can be identified in the EMS and GM units of the Sesia zone (Fig. 10). Eclogite high-pressure crystallization is recorded for some parts of the EMS unit at 85 ± 3 Ma. This event is preserved in white mica cores (Fig. 9; Halama et al., 2014) and in allanite (Regis et al., 2014). However, it is conspicuously absent in zircon, presumably because most zircons in high-pressure and ultrahigh-pressure rocks post-date peak pressures and mainly grow during late-stage exhumation and cooling (Kohn et al., 2015). It is followed by a selective metasomatic overprint at 75 ± 2 Ma (Fig. 10). In parts of the EMS unit, this age reflects the first high-pressure re-crystallization event (Regis et al., 2014; Giuntoli and Engi, 2016). A proposed decompression stage at ca. 68 Ma (Regis et al., 2014) is not recorded in our data set, possibly because of the different geological and structural histories of the different slices that make up the EMS unit. Subsequently, deformation-induced re-crystallization in the TSZ (Chiusella shear zone of Babist et al. [2006]) separating EMS from GM commenced at ca. 65 Ma as evidenced by a $^{40}Ar/^{39}Ar$ age of a mylonite (Halama et al., 2014), and various ages in EMS adjacent to the shear zone, including a Rb-Sr age (64.5 ± 1.5 Ma; Fig. 5F) and phengite core $^{40}Ar/^{39}Ar$ ages (Fig. 8F) presented here. Further north along the GM-EMS contact, this major phase of blueschist-facies deformation is dated at 60 ± 2 Ma, as indicated by the new Rb-Sr ages from the NSZ (samples MK-99 and MK-118, Figs. 5A, 5B). This may indicate prolonged phases of deformation of up to 5 m.y. with distinct intensities in various parts along the contact. Contemporaneous with the shearing along the GM-EMS contact, between ca. 65 and 60 Ma, there is a fluid influx into the EMS rocks that caused at least partial resetting of the Rb-Sr and K-Ar systems and is also recorded in the U-Pb system (e.g., Rubatto et al., 1999; Regis et al., 2014). Whereas these ages of 65–60 Ma reflect retrograde metamorphic conditions with respect to the EMS (Fig. 9), they reflect prograde conditions with respect to the GM, and $^{40}Ar/^{39}Ar$ phengite core ages in the greenschist-facies mylonites derived from the GM yield overlapping ages of 60.9 ± 0.4 Ma. Late increments of deformation and recrystallization along the TSZ, now under greenschist-facies conditions and structurally further toward the footwall, are constrained by our Rb-Sr maximum age for the end of deformation of 45–48 Ma. Published Rb-Sr ages of ca. 38–40 Ma from the GM (Inger et al., 1996) and a near-continuous spread of $^{40}Ar/^{39}Ar$ spot ages to values as low as ca. 33 Ma suggest that recrystallization continued in the GM until the end of the Eocene. This late greenschist-facies overprint is only observed in the GM but not in the investigated EMS samples. The geochronological results can be reconciled into a single *P-T* loop with various stages of (re-)crystallization related to fluid-rock interaction and deformation. Recrystallization appears to be episodic (clustering of ages around ca. 85, ca. 75, and 65–60 Ma) during the eclogite- and blueschist-facies stages but more or less continuous during the retrograde greenschist-facies stage. Cliff et al. (2017) emphasized that variations in temperature and pressure during metamorphism are continuous on a regional scale, but individual rocks may record discontinuous events related to strain migration or fluid ingress. The samples investigated record distinct recrystallization processes at different instants in an overall continuous metamorphic and structural evolution, but more data are required to fully evaluate the regional significance of the distinct recrystallization episodes.

CONCLUSIONS

The combination of Rb-Sr internal mineral isochrons and in situ $^{40}Ar/^{39}Ar$ data from samples representing different petrologic-structural stages provides geochronological information that can be linked together to improve our understanding of the temporal evolution of metamorphic rocks. In this study on rocks from the Sesia zone (Western Alps) that have experienced a complex history of continental subduction, we reach the following conclusions:

1. The abundant Sr isotope disequilibria between different sub-parageneses and the clear differences in $^{40}Ar/^{39}Ar$ spot ages related to step-like zoning in mineral chemistry demonstrate the lack of diffusive re-equilibration. The preservation of these disequilibrium features shows that deformation and fluid-induced metamorphic recrystallization control the isotopic signatures in these rocks.
2. Rb-Sr internal mineral isochrons of the blueschist-facies mylonites record Rb-Sr re-equilibration at ca. 60 Ma in the major shear zone that separates the two key lithological units in the Sesia zone, the eclogitic micaschists and the *gneiss minuti*. Local reactivation and recrystallization within this shear zone lasted for at least ~15 m.y.
3. Distinct sets of Rb-Sr age information can be obtained from single samples that experienced several stages of deformation and recrystallization and comprise sub-parageneses of mineral assemblages. Different white mica populations show systematic variations of Rb-Sr signatures. Large white mica grain size fractions together with low-Rb/Sr phases with the

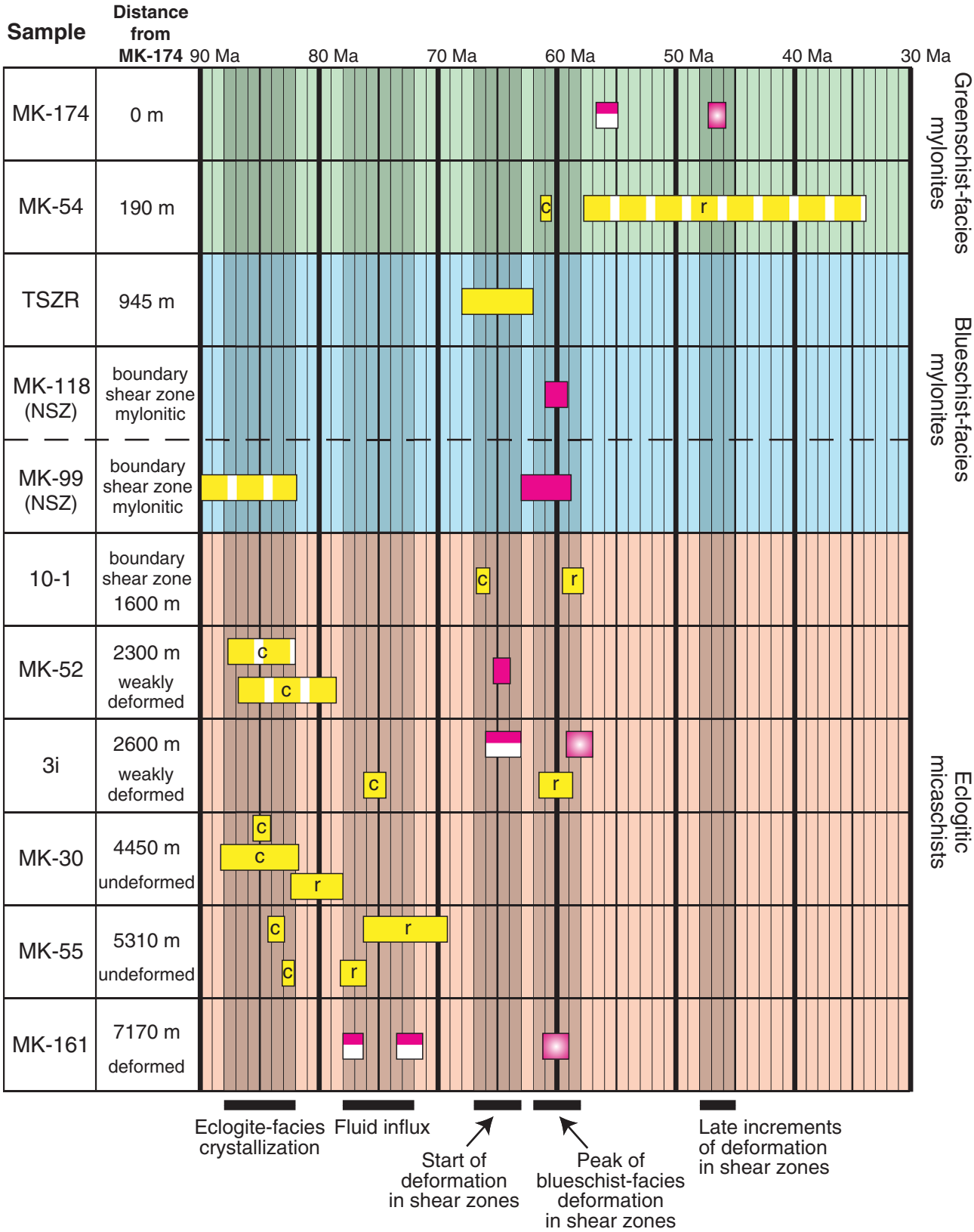

Figure 10. Compilation of the Rb-Sr and $^{40}Ar/^{39}Ar$ ages obtained in this study and the accompanying study by Halama et al. (2014, samples TSZR, MK-30, MK-52 and MK-55), and their structural position in relation to the shear zones separating the eclogitic micaschists from the *gneiss minuti*. The Rb-Sr age for sample MK-52 is from Babist et al. (2006). NSZ—Nantay shear zone. No distance provided for samples MK-118 and MK-99 because they have been projected from the NSZ onto this profile.

lowest $^{87}Sr/^{86}Sr$ ratios define minimum ages of relict assemblage crystallization. Fine white mica fractions and low-Rb/Sr phases that recrystallized with higher $^{87}Sr/^{86}Sr$ ratios due to radiogenic ingrowth of ^{87}Sr provide age constraints on the timing of the late increments of deformation.

4. The comparison of geochronological data from the Rb-Sr and $^{40}Ar/^{39}Ar$ systems reveals two characteristic relationships: Rb-Sr isochron ages of relict assemblages match $^{40}Ar/^{39}Ar$ phengite core ages, and Rb-Sr isochron ages of deformation assemblages concur with $^{40}Ar/^{39}Ar$ ages from overprinted phengite rims. However, in weakly deformed rocks with limited fluid-rock interaction, relict $^{40}Ar/^{39}Ar$ domains yielding older apparent ages not recorded by the Rb-Sr system may be preserved.

ACKNOWLEDGMENTS

We thank Christine Fischer for help with sample preparation. We also thank Bob Cliff and an anonymous reviewer for their constructive comments that helped to improve the manuscript. We greatly appreciate the editorial handling by Phillipe Agard, who also provided helpful advice on improving the structure and clarity of the manuscript. Funding of this work by the Deutsche Forschungsgemeinschaft (grant KO-3750/2) is gratefully acknowledged.

REFERENCES CITED

Agard, P., Monié, P., Jolivet, L., and Goffé, B., 2002, Exhumation of the Schistes Lustrés complex: *In situ* laser probe $^{40}Ar/^{39}Ar$ constraints and implications for the Western Alps: Journal of Metamorphic Geology, v. 20, p. 599–618, https://doi.org/10.1046/j.1525-1314.2002.00391.x.

Altherr, R., Schliestedt, M., Okrusch, M., Siedel, E., Kreuzer, H., Harre, W., Lenz, H., Wendt, I., and Wagner, G.A., 1979, Geochronology of high pressure rocks on Sifnos (Cyclades, Greece): Contributions to Mineralogy and Petrology, v. 70, p. 245–255, https://doi.org/10.1007/BF00375354.

Angiboust, S., Glodny, J., Oncken, O., and Chopin, C., 2014, In search of transient subduction interfaces in the Dent Blanche–Sesia Tectonic System (W. Alps): Lithos, v. 205, p. 298–321, https://doi.org/10.1016/j.lithos.2014.07.001.

Angiboust, S., Agard, P., Glodny, J., Omrani, J., and Oncken, O., 2016, Zagros blueschists: Episodic underplating and long-lived cooling of a subduction zone: Earth and Planetary Science Letters, v. 443, p. 48–58, https://doi.org/10.1016/j.epsl.2016.03.017.

Babist, J., Handy, M.R., Konrad-Schmolke, M., and Hammerschmidt, K., 2006, Precollisional, multistage exhumation of subducted continental crust: The Sesia Zone, western Alps: Tectonics, v. 25, TC6008, https://doi.org/10.1029/2005TC001927.

Baksi, A.K., 1999, Reevaluation of plate motion models based on hotspot tracks in the Atlantic and Indian Oceans: The Journal of Geology, v. 107, p. 13–26, https://doi.org/10.1086/314329.

Baksi, A.K., 2006, Guidelines for assessing the reliability of $^{40}Ar/^{39}Ar$ plateau ages: Application to ages relevant to hotspot tracks: http://www.mantleplumes.org/ArAr.html (accessed February 2017).

Baxter, E.F., 2010, Diffusion of noble gases in minerals: Reviews in Mineralogy and Geochemistry, v. 72, p. 509–557, https://doi.org/10.2138/rmg.2010.72.11.

Beltrando, M., Lister, G.S., Forster, M., Dunlap, W.J., Fraser, G., and Hermann, J., 2009, Dating microstructures by the $^{40}Ar/^{39}Ar$ step-heating technique: Deformation-pressure-temperature-time history of the Penninic units of the Western Alps: Lithos, v. 113, p. 801–819, https://doi.org/10.1016/j.lithos.2009.07.006.

Beltrando, M., Compagnoni, R., and Lombardo, B., 2010, (Ultra-) High-pressure metamorphism and orogenesis: An Alpine perspective: Gondwana Research, v. 18, p. 147–166, https://doi.org/10.1016/j.gr.2010.01.009.

Berger, A., Thomsen, T.B., Ovtcharova, M., Kapferer, N., and Mercolli, I., 2012, Dating emplacement and evolution of the orogenic magmatism in the internal Western Alps: 1. The Miagliano Pluton: Swiss Journal of Geosciences, v. 105, p. 49–65, https://doi.org/10.1007/s00015-012-0091-7.

Boundy, T.M., Hall, C.M., Li, G., Essene, E.J., and Halliday, A.N., 1997, Fine-scale isotopic heterogeneities and fluids in the deep crust: A $^{40}Ar/^{39}Ar$ laser ablation and TEM study of muscovites from a granulite-eclogite transition zone: Earth and Planetary Science Letters, v. 148, p. 223–242, https://doi.org/10.1016/S0012-821X(97)00036-8.

Bröcker, M., and Franz, L., 1998, Rb-Sr isotope studies on Tinos Island (Cyclades, Greece): Additional time constraints for metamorphism, extent of infiltration-controlled overprinting and deformational activity: Geological Magazine, v. 135, p. 369–382, https://doi.org/10.1017/S0016756898008681.

Bröcker, M., and Franz, L., 2005, The base of the Cycladic blueschist unit on Tinos Island (Greece) re-visited: Field relationships, phengite chemistry and Rb-Sr geochronology: Neues Jahrbuch für Mineralogie: Abhandlungen, v. 181, p. 81–93, https://doi.org/10.1127/0077-7757/2005/0181-0003.

Bröcker, M., Baldwin, S., and Arkudas, R., 2013, The geological significance of $^{40}Ar/^{39}Ar$ and Rb-Sr white mica ages from Syros and Sifnos, Greece: A record of continuous (re)crystallization during exhumation?: Journal of Metamorphic Geology, v. 31, p. 629–646, https://doi.org/10.1111/jmg.12037.

Charlier, B.L.A., Ginibre, C., Morgan, D., Nowell, G.M., Pearson, D.G., Davidson, J.P., and Ottley, C.J., 2006, Methods for the microsampling and high-precision analysis of strontium and rubidium isotopes at single crystal scale for petrological and geochronological applications: Chemical Geology, v. 232, p. 114–133, https://doi.org/10.1016/j.chemgeo.2006.02.015.

Chen, C.H., DePaolo, D.J., and Lan, C.Y., 1996, Rb-Sr microchrons in the Manaslu granite: Implications for Himalayan thermochronology: Earth and Planetary Science Letters, v. 143, p. 125–135, https://doi.org/10.1016/0012-821X(96)00122-7.

Cherniak, D.J., 1997, An experimental study of strontium and lead diffusion in calcite, and implications for carbonate diagenesis and metamorphism: Geochimica et Cosmochimica Acta, v. 61, p. 4173–4179, https://doi.org/10.1016/S0016-7037(97)00236-6.

Cliff, R.A., and Meffan-Main, S., 2003, Evidence from Rb-Sr microsampling geochronology for the timing of Alpine deformation in the Sonnblick Dome, SE Tauern Window, Austria, *in* Vance, D., Müller, W., and Villa, I.M., eds., Geochronology: Linking the Isotopic Record with Petrology and Textures: Geological Society of London Special Publication 220, p. 159–172, https://doi.org/10.1144/GSL.SP.2003.220.01.09.

Cliff, R.A., Bond, C.E., Butler, R.W.H., and Dixon, J.E., 2017, Geochronological challenges posed by continuously developing tectonometamorphic systems: Insights from Rb-Sr mica ages from the Cycladic Blueschist Belt, Syros (Greece): Journal of Metamorphic Geology, v. 35, p. 197–211, https://doi.org/10.1111/jmg.12228.

Compagnoni, R., Dal Piaz, G.V., Hunziker, J.C., Gosso, G., Lombardo, B., and Williams, P.F., 1977, The Sesia-Lanzo Zone, a slice of continental crust with Alpine high pressure–low temperature assemblages in the Western Italian Alps: Rendiconti della Società Italiana di Mineralogia e Petrologia, v. 33, p. 281–334.

Cortiana, G., Dal Piaz, G.V., Del Moro, A., Hunziker, J.C., and Martin, S., 1998, ^{40}Ar-^{39}Ar and Rb-Sr dating of the Pillonet klippe and Sesia-Lanzo basal slice in the Ayas valley and evolution of the Austroalpine-Piedmont nappe stack: Memorie di Scienze Geologiche, v. 50, p. 177–194.

Cumbest, R.J., Johnson, E.L., and Onstott, T.C., 1994, Argon composition of metamorphic fluids: Implications for $^{40}Ar/^{39}Ar$ geochronology: Geological Society of America Bulletin, v. 106, p. 942–951, https://doi.org/10.1130/0016-7606(1994)106<0942:ACOMFI>2.3.CO;2.

Dal Piaz, G.V., Gosso, G., and Martinotti, G., 1971, La II Zona Diorito-kinzigitica tra la Valsesia e la Valle d'Ayas (Alpi occidentali): Memorie della Societa Geologica Italiana, v. 10, p. 257–276.

Dal Piaz, G.V., Hunziker, J.C., and Martinotti, G., 1972, La zona Sesia-Lanzo e l'evoluzione tettonico-metamorfica delle Alpi nordoccidentali interne: Memorie della Societa Geologica Italiana, v. 11, p. 433–466.

Di Vincenzo, G., and Palmeri, R., 2001, An ^{40}Ar-^{39}Ar investigation of high-pressure metamorphism and the retrogressive history of mafic eclogites from the Lanterman Range (Antarctica): Evidence against a simple temperature control on argon transport in amphibole: Contributions to Mineralogy and Petrology, v. 141, p. 15–35, https://doi.org/10.1007/s004100000226.

Di Vincenzo, G., Ghiribelli, B., Giorgetti, G., and Palmeri, R., 2001, Evidence of a close link between petrology and isotope records: Constraints from SEM, EMP, TEM and in situ ^{40}Ar-^{39}Ar laser analyses on multiple generations of white micas (Lanterman Range, Antarctica): Earth and Planetary Science Letters, v. 192, p. 389–405, https://doi.org/10.1016/S0012-821X(01)00454-X.

Di Vincenzo, G., Tonarini, S., Lombardo, B., Castelli, D., and Ottolini, L., 2006, Comparison of ^{40}Ar-^{39}Ar and Rb-Sr data on phengites from the UHP Brossasco-Isasca unit (Dora Maira Massif,

Italy): Implications for dating white mica: Journal of Petrology, v. 47, p. 1439–1465, https://doi.org/10.1093/petrology/egl018.
Dresen, G., Evans, B., and Olgaard, D.L., 1998, Effect of quartz inclusions on plastic flow in marble: Geophysical Research Letters, v. 25, p. 1245–1248, https://doi.org/10.1029/98GL00730.
Duchêne, S., Blichert-Toft, J., Luais, B., Télouk, P., Lardeaux, J.-M., and Albarède, F., 1997, The Lu-Hf dating of garnets and the ages of the Alpine high-pressure metamorphism: Nature, v. 387, p. 586–589, https://doi.org/10.1038/42446.
Freeman, S.R., Inger, S., Butler, R.W.H., and Cliff, R.A., 1997, Dating deformation using Rb-Sr in white mica: Greenschist facies deformation ages from the Entrelor shear zone, Italian Alps: Tectonics, v. 16, p. 57–76, https://doi.org/10.1029/96TC02477.
Freeman, S.R., Butler, R.W.H., Cliff, R.A., and Rex, D.C., 1998, Direct dating of mylonite evolution: A multi-disciplinary geochronological study from the Moine Thrust Zone, NW Scotland: Journal of the Geological Society, v. 155, p. 745–758, https://doi.org/10.1144/gsjgs.155.5.0745.
Giuntoli, F., and Engi, M., 2016, Internal geometry of the central Sesia Zone (Aosta Valley, Italy): HP tectonic assembly of continental slices: Swiss Journal of Geosciences, v. 109, p. 445–471, https://doi.org/10.1007/s00015-016-0225-4.
Giuntoli, F., Lanari, P., and Engi, M., 2018a, Deeply subducted continental fragments—Part 1: Fracturing, dissolution-precipitation, and diffusion processes recorded by garnet textures of the central Sesia Zone (western Italian Alps): Solid Earth, v. 9, p. 167–189, https://doi.org/10.5194/se-9-167-2018.
Giuntoli, F., Lanari, P., Burn, M., Kunz, B.E., and Engi, M., 2018b, Deeply subducted continental fragments—Part 2: Insight from petrochronology in the central Sesia Zone (western Italian Alps): Solid Earth, v. 9, p. 191–222, https://doi.org/10.5194/se-9-191-2018.
Glodny, J., Bingen, B., Austrheim, H., Molina, J.F., and Rusin, A., 2002, Precise eclogitization ages deduced from Rb/Sr mineral systematics: The Maksyutov complex, Southern Urals, Russia: Geochimica et Cosmochimica Acta, v. 66, p. 1221–1235, https://doi.org/10.1016/S0016-7037(01)00842-0.
Glodny, J., Austrheim, H., Molina, J.F., Rusin, A.I., and Seward, D., 2003, Rb/Sr record of fluid-rock interaction in eclogites: The Marun-Keu complex, Polar Urals, Russia: Geochimica et Cosmochimica Acta, v. 67, p. 4353–4371, https://doi.org/10.1016/S0016-7037(03)00370-3.
Glodny, J., Ring, U., and Kühn, A., 2008a, Coeval high-pressure metamorphism, thrusting, strike-slip, and extensional shearing in the Tauern Window, Eastern Alps: Tectonics, v. 27, TC4004, https://doi.org/10.1029/2007TC002193.
Glodny, J., Kühn, A., and Austrheim, H., 2008b, Geochronology of fluid-induced eclogite and amphibolite facies metamorphic reactions in a subduction-collision system, Bergen Arcs, Norway: Contributions to Mineralogy and Petrology, v. 156, p. 27–48, https://doi.org/10.1007/s00410-007-0272-y.
Halama, R., and Konrad-Schmolke, M., 2015, Retrograde metasomatic effects on phase assemblages in an interlayered blueschist-greenschist sequence (Coastal Cordillera, Chile): Lithos, v. 216–217, p. 31–47, https://doi.org/10.1016/j.lithos.2014.12.004.
Halama, R., Konrad-Schmolke, M., Sudo, M., Marschall, H.R., and Wiedenbeck, M., 2014, Effects of fluid-rock interaction on $^{40}Ar/^{39}Ar$ geochronology in high-pressure rocks (Sesia-Lanzo Zone, Western Alps): Geochimica et Cosmochimica Acta, v. 126, p. 475–494, https://doi.org/10.1016/j.gca.2013.10.023.
Harrison, T.M., Célérier, J., Aikman, A.B., Hermann, J., and Heizler, M.T., 2009, Diffusion of ^{40}Ar in muscovite: Geochimica et Cosmochimica Acta, v. 73, p. 1039–1051, https://doi.org/10.1016/j.gca.2008.09.038.
Inger, S., and Cliff, R.A., 1994, Timing of metamorphism in the Tauern Window, Eastern Alps: Rb-Sr ages and fabric formation: Journal of Metamorphic Geology, v. 12, p. 695–707, https://doi.org/10.1111/j.1525-1314.1994.tb00052.x.
Inger, S., Ramsbotham, W., Cliff, R.A., and Rex, D.C., 1996, Metamorphic evolution of the Sesia-Lanzo Zone, Western Alps: Time constraints from multi-system geochronology: Contributions to Mineralogy and Petrology, v. 126, p. 152–168, https://doi.org/10.1007/s004100050241.
Itaya, T., Tsujimori, T., and Liou, J.G., 2011, Evolution of the Sanbagawa and Shimanto high-pressure belts in SW Japan: Insights from K-Ar (Ar-Ar) geochronology: Journal of Asian Earth Sciences, v. 42, p. 1075–1090, https://doi.org/10.1016/j.jseaes.2011.06.012.
Kalsbeek, F., and Hansen, M., 1989, Statistical analysis of Rb-Sr isotope data by the "bootstrap" method: Chemical Geology: Isotope Geoscience Section, v. 73, p. 289–297, https://doi.org/10.1016/0168-9622(89)90022-5.
Kelley, S., 2002, Excess argon in K-Ar and Ar-Ar geochronology: Chemical Geology, v. 188, p. 1–22, https://doi.org/10.1016/S0009-2541(02)00064-5.
Kohn, M.J., Corrie, S.L., and Markley, C., 2015, The fall and rise of metamorphic zircon: The American Mineralogist, v. 100, p. 897–908, https://doi.org/10.2138/am-2015-5064.
Konrad-Schmolke, M., and Halama, R., 2014, Combined thermodynamic-geochemical modeling in metamorphic geology: Boron as tracer of fluid-rock interaction: Lithos, v. 208–209, p. 393–414, https://doi.org/10.1016/j.lithos.2014.09.021.
Konrad-Schmolke, M., Babist, J., Handy, M.R., and O'Brien, P.J., 2006, The physico-chemical properties of a subducted slab from garnet zonation patterns (Sesia Zone, Western Alps): Journal of Petrology, v. 47, p. 2123–2148, https://doi.org/10.1093/petrology/egl039.
Konrad-Schmolke, M., O'Brien, P.J., and Zack, T., 2011a, Fluid migration above a subducted slab: Constraints on amount, pathways and major element mobility from partially overprinted eclogite-facies rocks (Sesia Zone, Western Alps): Journal of Petrology, v. 52, p. 457–486, https://doi.org/10.1093/petrology/egq087.
Konrad-Schmolke, M., Zack, T., O'Brien, P.J., and Barth, M., 2011b, Fluid migration above a subducted slab: Thermodynamic and trace element modelling of fluid-rock interaction in partially overprinted eclogite-facies rocks (Sesia Zone, Western Alps): Earth and Planetary Science Letters, v. 311, p. 287–298, https://doi.org/10.1016/j.epsl.2011.09.025.
Krohe, A., and Wawrzenitz, N., 2000, Domainal variations of U-Pb monazite ages and Rb-Sr whole-rock dates in polymetamorphic paragneisses (KTB Drill Core, Germany): Influence of strain and deformation mechanisms on isotope systems: Journal of Metamorphic Geology, v. 18, p. 271–291, https://doi.org/10.1046/j.1525-1314.2000.00255.x.
Kuiper, Y.D., 2002, The interpretation of inverse isochron diagrams in $^{40}Ar/^{39}Ar$ geochronology: Earth and Planetary Science Letters, v. 203, p. 499–506, https://doi.org/10.1016/S0012-821X(02)00833-6.
Lanphere, M.A., and Baadsgaard, H., 2001, Precise K-Ar, $^{40}Ar/^{39}Ar$, Rb-Sr and U/Pb mineral ages from the 27.5 Ma Fish Canyon Tuff reference standard: Chemical Geology, v. 175, p. 653–671, https://doi.org/10.1016/S0009-2541(00)00291-6.
Lardeaux, J.-M., Gosso, G., Kienast, J.R., and Lombardo, B., 1982, Relations entre le métamorphisme et al deformation dans la zone Sésia-Lanzo (Alpes Occidentales) et le problème de l'éclogitisation de la croute continentale: Bulletin de la Société Geologique de France, v. 24, p. 793–800, https://doi.org/10.2113/gssgfbull.S7-XXIV.4.793.
Ludwig, K.R., 2009, Isoplot/Ex ver 3.71: A geochronological toolkit for Microsoft Excel: Berkeley Geochronology Center Special Publication 4, 77 p.
Menold, C.A., Grove, M., Sievers, N.E., Manning, C.E., Yin, A., Young, E.D., and Ziegler, K., 2016, Argon, oxygen, and boron isotopic evidence documenting $^{40}Ar_E$ accumulation in phengite during water-rich high-pressure subduction metasomatism of continental crust: Earth and Planetary Science Letters, v. 446, p. 56–67, https://doi.org/10.1016/j.epsl.2016.04.010.
Mulch, A., Cosca, M., and Handy, M., 2002, In-situ UV-laser $^{40}Ar/^{39}Ar$ geochronology of a micaceous mylonite: An example of defect-enhanced argon loss: Contributions to Mineralogy and Petrology, v. 142, p. 738–752, https://doi.org/10.1007/s00410-001-0325-6.
Mulch, A., Cosca, M.A., Andresen, A., and Fiebig, J., 2005, Time scales of deformation and exhumation in extensional detachment systems determined by high-spatial resolution in situ UV-laser $^{40}Ar/^{39}Ar$ dating: Earth and Planetary Science Letters, v. 233, p. 375–390, https://doi.org/10.1016/j.epsl.2005.01.042.
Müller, W., Dallmeyer, R.D., Neubauer, F., and Thöni, M., 1999, Deformation-induced resetting of Rb/Sr and $^{40}Ar/^{39}Ar$ mineral systems in a low-grade, polymetamorphic terrane (Eastern Alps, Austria): Journal of the Geological Society, v. 156, p. 261–278, https://doi.org/10.1144/gsjgs.156.2.0261.
Müller, W., Mancktelow, N.S., and Meier, M., 2000, Rb-Sr microchrons of synkinematic mica in mylonites: An example from the DAV fault of the Eastern Alps: Earth and Planetary Science Letters, v. 180, p. 385–397, https://doi.org/10.1016/S0012-821X(00)00167-9.
Nier, A.O., 1950, A redetermination of the relative abundances of the isotopes of carbon, nitrogen, oxygen, argon, and potassium: Physical Review, v. 77, p. 789–793, https://doi.org/10.1103/PhysRev.77.789.
Oberhänsli, R., Hunziker, J.C., Martinotti, G., and Stern, W.B., 1985, Geochemistry, geochronology and petrology of Monte Mucrone: An example of Eo-Alpine eclogitization of Permian granitoids in the Sesia-Lanzo Zone, Western Alps, Italy: Chemical Geology: Isotope Geoscience Section, v. 52, p. 165–184, https://doi.org/10.1016/0168-9622(85)90016-8.
Pognante, U., Talarico, F., Rastelli, N., and Ferrati, N., 1987, High pressure metamorphism in the nappes of the Valle dell'Orco traverse (Western Alps collisional belt): Journal of Metamorphic Geology, v. 5, p. 397–414, https://doi.org/10.1111/j.1525-1314.1987.tb00392.x.
Proyer, A., 2003, The preservation of high-pressure rocks during exhumation: Metagranites and metapelites: Lithos, v. 70, p. 183–194, https://doi.org/10.1016/S0024-4937(03)00098-7.

Putlitz, B., Cosca, M.A., and Schumacher, J.C., 2005, Prograde mica $^{40}Ar/^{39}Ar$ growth ages recorded in high pressure rocks (Syros, Cyclades, Greece): Chemical Geology, v. 214, p. 79–98, https://doi.org/10.1016/j.chemgeo.2004.08.056.

Putnis, A., 2009, Mineral replacement reactions: Reviews in Mineralogy and Geochemistry, v. 70, p. 87–124, https://doi.org/10.2138/rmg.2009.70.3.

Regis, D., Rubatto, D., Darling, J., Cenki-Tok, B., Zucali, M., and Engi, M., 2014, Multiple metamorphic stages within an eclogite-facies terrane (Sesia Zone, Western Alps) revealed by Th-U-Pb petrochronology: Journal of Petrology, v. 55, p. 1429–1456, https://doi.org/10.1093/petrology/egu029.

Ridley, J., 1989, Structural and metamorphic history of a segment of the Sesia-Lanzo zone, and its bearing on the kinematics of Alpine deformation in the western Alps, *in* Coward, M.P., Dietrich, D., and Park, R.G., eds., Alpine Tectonics: Geological Society of London Special Publication 45, p. 189–201, https://doi.org/10.1144/GSL.SP.1989.045.01.10.

Romer, R.L., and Rötzler, J., 2011, The role of element distribution for the isotopic dating of metamorphic minerals: European Journal of Mineralogy, v. 23, p. 17–33, https://doi.org/10.1127/0935-1221/2011/0023-2081.

Rubatto, D., Gebauer, D., and Compagnoni, R., 1999, Dating of eclogite-facies zircons: The age of Alpine metamorphism in the Sesia-Lanzo Zone (Western Alps): Earth and Planetary Science Letters, v. 167, p. 141–158, https://doi.org/10.1016/S0012-821X(99)00031-X.

Rubatto, D., Regis, D., Hermann, J., Boston, K., Engi, M., Beltrando, M., and McAlpine, S.R.B., 2011, Yo-yo subduction recorded by accessory minerals in the Italian Western Alps: Nature Geoscience, v. 4, p. 338–342, https://doi.org/10.1038/ngeo1124.

Ruffet, G., Féraud, G., Ballèvre, M., and Kiénast, J.-R., 1995, Plateau ages and excess argon in phengites: An ^{40}Ar-^{39}Ar laser probe study of Alpine micas (Sesia Zone, Western Alps, northern Italy): Chemical Geology: Isotope Geoscience Section, v. 121, p. 327–343, https://doi.org/10.1016/0009-2541(94)00132-R.

Ruffet, G., Gruau, G., Ballèvre, M., Féraud, G., and Philippot, P., 1997, Rb-Sr and ^{40}Ar-^{39}Ar laser probe dating of high-pressure phengites from the Sesia zone (Western Alps): Underscoring of excess argon and new age constraints on the high-pressure metamorphism: Chemical Geology, v. 141, p. 1–18, https://doi.org/10.1016/S0009-2541(97)00052-1.

Scaillet, S., Féraud, G., Lagabrielle, Y., Ballèvre, M., and Ruffet, G., 1990, $^{40}Ar/^{39}Ar$ laser-probe dating by step heating and spot fusion of phengites from the Dora Maira nappe of the western Alps, Italy: Geology, v. 18, p. 741–744, https://doi.org/10.1130/0091-7613(1990)018<0741:AALPDB>2.3.CO;2.

Schneider, S., Hammerschmidt, K., and Rosenberg, C.L., 2013, Dating the longevity of ductile shear zones: Insight from $^{40}Ar/^{39}Ar$ in situ analyses: Earth and Planetary Science Letters, v. 369–370, p. 43–58, https://doi.org/10.1016/j.epsl.2013.03.002.

Sherlock, S., and Kelley, S., 2002, Excess argon evolution in HP-LT rocks: A UVLAMP study of phengite and K-free minerals, NW Turkey: Chemical Geology, v. 182, p. 619–636, https://doi.org/10.1016/S0009-2541(01)00345-X.

Sousa, J., Kohn, M.J., Schmitz, M.D., Northrup, C.J., and Spear, F.S., 2013, Strontium isotope zoning in garnet: Implications for metamorphic matrix equilibration, geochronology and phase equilibrium modelling: Journal of Metamorphic Geology, v. 31, p. 437–452, https://doi.org/10.1111/jmg.12028.

Steiger, R.H., and Jäger, E., 1977, Submission on geochronology: Convention on the use of decay constants in geo- and cosmochronology: Earth and Planetary Science Letters, v. 36, p. 359–362, https://doi.org/10.1016/0012-821X(77)90060-7.

Uto, K., Ishizuka, O., Matsumoto, A., Kamioka, H., and Togashi, S., 1997, Laser-heating $^{40}Ar/^{39}Ar$ dating system of the Geological Survey of Japan: System outline and preliminary results: Bulletin of the Geological Survey of Japan, v. 48, p. 23–46.

Venturini, G., Martinotti, G., Armando, G., Barbero, M., and Hunziker, J.C., 1994, The central Sesia Lanzo Zone (Western Italian Alps): New field observations and lithostratigraphic subdivisions: Schweizerische Mineralogische und Petrographische Mitteilungen, v. 74, p. 115–125.

Villa, I.M., 1998, Isotopic closure: Terra Nova, v. 10, p. 42–47, https://doi.org/10.1046/j.1365-3121.1998.00156.x.

Villa, I.M., 2010, Disequilibrium textures versus equilibrium modelling: Geochronology at the crossroads, *in* Spalla, M.I., Marotta, A.M., and Gosso, G., eds., Advances in Interpretation of Geological Processes: Refinement of Multi-Scale Data and Integration in Numerical Modelling: Geological Society of London Special Publication 332, p. 1–15, https://doi.org/10.1144/SP332.1.

Villa, I.M., 2016, Diffusion in mineral geochronometers: Present and absent: Chemical Geology, v. 420, p. 1–10, https://doi.org/10.1016/j.chemgeo.2015.11.001.

Villa, I.M., Bucher, S., Bousquet, R., Kleinhanns, I.C., and Schmid, S.M., 2014, Dating polygenetic metamorphic assemblages along a transect across the Western Alps: Journal of Petrology, v. 55, p. 803–830, https://doi.org/10.1093/petrology/egu007.

Villa, I.M., De Bièvre, P., Holden, N.E., and Renne, P.R., 2015, IUPAC-IUGS recommendation on the half life of ^{87}Rb: Geochimica et Cosmochimica Acta, v. 164, p. 382–385, https://doi.org/10.1016/j.gca.2015.05.025.

Walker, S., Thirlwall, M.F., Strachan, R.A., and Bird, A.F., 2016, Evidence from Rb-Sr mineral ages for multiple orogenic events in the Caledonides of Shetland, Scotland: Journal of the Geological Society, v. 173, p. 489–503, https://doi.org/10.1144/jgs2015-034.

Warren, C.J., Sherlock, S.C., and Kelley, S.P., 2011, Interpreting high-pressure phengite $^{40}Ar/^{39}Ar$ laserprobe ages: An example from Saih Hatat, NE Oman: Contributions to Mineralogy and Petrology, v. 161, p. 991–1009, https://doi.org/10.1007/s00410-010-0576-1.

Warren, C.J., Kelley, S.P., Sherlock, S.C., and McDonald, C.S., 2012a, Metamorphic rocks seek meaningful cooling rate: Interpreting $^{40}Ar/^{39}Ar$ ages in an exhumed ultra-high pressure terrane: Lithos, v. 155, p. 30–48, https://doi.org/10.1016/j.lithos.2012.08.011.

Warren, C.J., Smye, A.J., Kelley, S.P., and Sherlock, S.C., 2012b, Using white mica $^{40}Ar/^{39}Ar$ data as a tracer for fluid flow and permeability under high-P conditions: Tauern Window, Eastern Alps: Journal of Metamorphic Geology, v. 30, p. 63–80, https://doi.org/10.1111/j.1525-1314.2011.00956.x.

Wendt, I., and Carl, C., 1991, The statistical distribution of the mean squared weighted deviation: Chemical Geology: Isotope Geoscience Section, v. 86, p. 275–285, https://doi.org/10.1016/0168-9622(91)90010-T.

Wiederkehr, M., Sudo, M., Bousquet, R., Berger, A., and Schmid, S.M., 2009, Alpine orogenic evolution from subduction to collisional thermal overprint: The $^{40}Ar/^{39}Ar$ age constraints from the Valaisan Ocean, central Alps: Tectonics, v. 28, TC6009, https://doi.org/10.1029/2009TC002496.

Willner, A.P., Sepúlveda, F.A., Hervé, F., Massonne, H.-J., and Sudo, M., 2009, Conditions and timing of pumpellyite-actinolite facies metamorphism in the early Mesozoic frontal accretionary prism of the Madre de Dios Archipelago (latitude 50°20′S; southern Chile): Journal of Petrology, v. 50, p. 2127–2155, https://doi.org/10.1093/petrology/egp071.